The Network Strain Filter - A New Tool for Monitoring and Detecting Transient Deformation Signals in GPS Arrays

Ryu Ohtani

Geological Survey of Japan, National Institute of Advanced Industrial Science and Technology, Tsukuba, Japan

Jeffrey J. McGuire

Woods Hole Oceanographic Institution, Woods Hole, Massachusetts

Paul Segall

Department of Geophysics, Stanford University, California

Abstract. We have developed a tool to detect transient deformation signals from large-scale (principally GPS) geodetic arrays, referred to as a Network Strain Filter (NSF). The strategy is to extract spatially and temporally coherent signals by analyzing data from entire geodetic networks simultaneously. The NSF models GPS displacement time series as a sum of contributions from: secular motion, transient displacements, site-specific local benchmark motion, reference frame errors, and white noise. Transient displacements are represented by a spatial wavelet basis with temporally-varying coefficients that are estimated with a Kalman filter. A temporal smoothing parameter is also estimated on-line by the filter. The problem is regularized in the spatial domain by minimizing a smoothing (Laplacian) norm of the transient strain-rate field. To test the performance of the NSF, we carried out numerical tests using the southern California Integrated GPS Network (SCIGN) station distribution and a 3 year long synthetic transient in a 6 year time series. We demonstrate that the NSF can identify the transient signal, even when the colored noise amplitude is comparable to that of transient signal.

Application of the method to actual GPS data from the Japanese GPS network (GEONET) on the Boso Peninsula, also shows that the NSF can detect transient motions resulting from aseismic fault slip.

1. Introduction

In the past decade there has been a tremendous increase in the number and density of geodetic networks for the study of crustal deformation. Large-scale permanent GPS arrays have been developed in Japan (GEONET) [Hatanaka et al., 2003], southern California [Hudnut et al., 2002], the Basin and Range (BARGEN) [Niemi et al., 2004], the Pacific Northwest (PANGA) [Miller et al., 2002], the San Francisco Bay region (BARD) [see, for example, http://gcmd.nasa.gov/records/GCMD_BARD-GPS.html], and elsewhere. In the western United States, 875 continuous GPS receivers are operated by the Plate Boundary Observatory (PBO) as part of the National Science Foundation Earthscope Initiative [for details, see http://pboweb.unavco.org/]. These GPS networks yield daily estimates of site positions with a precision of 1 to 2 millimeters in the horizontal and 3-4 mm in the vertical over regional distances [e.g., Zhang et al., 1997], and are for the first time providing deformation measurements dense in both space and time. Networks of borehole tiltmeters [Hirose et al, 2005] and strainmeters [Wang et al., 2008] provide greater sensitivity at periods shorter than a few weeks, and have yielded significant insights into transient processes [e.g., Hirose et al., 2005; Hirose et al., 2006].

For some time, much of the geophysical GPS community's research effort has focused on obtaining accurate interseismic velocities and coseismic displacements [which are reviewed in, for example, Segall and Davis, 1997; Sagiya, 2004]. More recently, transient deformation events have received a great deal of attention. These observations

46 can be modeled as resulting from slip on faults with a rupture velocity much less than the
47 shear wave velocity. Because these so-called slow slip events are nominally invisible to
48 seismic instrumentation yet may release significant elastic strain, they have become the
49 subject of great scientific interest. Slow slip events have now been discovered in Japan
50 [Hirose et al, 1999; Ozawa et al, 2001; Miyazaki et al, 2003; Ozawa et al; 2002;
51 Miyazaki et al, 2006], the Cascadia subduction zone [Dragert et. al, 2001; Miller et al,
52 2002; Szeliga et al, 2008], Mexico [Lowry et al., 2001; Kostoglodov et al, 2003; Larson
53 et al, 2007], Central America [Norabuena et al., 2004], New Zealand [Douglas, 2005;
54 McCaffrey et al, 2008; Delahaye et al, 2009], and beneath Kilauea volcano in Hawaii
55 [Cervelli et. al., 2002; Segall et al, 2006; Brooks et al, 2006]. It is now recognized that
56 slow slip events in Cascadia and Japan are accompanied by 1-5 Hz seismic signals
57 referred to as "non-volcanic tremor" [Rogers and Dragert, 2003; Obara, 2002; Shelly et al,
58 2007]. The moment magnitudes of these events range from Mw 5.7 beneath Kilauea to
59 greater than Mw 7 in some of the subduction zone events. The durations of these events
60 also vary considerably; the Bungo Channel event in southwest Japan lasted roughly one
61 year, the Cascadia slow slip event several weeks, the Kilauea silent slip event only one to
62 two days, while the Tokai gap, Japan slow slip event lasted roughly 6 years [Miyazaki et
63 al, 2006]. The Cascadia events are known to be episodic, with repeat times of 11 to 18
64 months (Brudzinski and Allen, 2007; Schwartz and Rokosky, 2007). Previously, slow
65 earthquakes have been identified on the San Andreas Fault from strain and creepmeter
66 recordings [Linde et. al., 1996].

67 Transient post-seismic deformation is also well established [eg, Heki et. al., 1997;
68 Hsu et al, 2007; Pritchard and Simons, 2006]. Deformation in volcanic regions is well

69 known to be episodic, with transient strains preceding some volcanic eruptions. The time
70 scales of pre-eruptive deformation, however, can be quite variable. For example,
71 permanent GPS stations on Kilauea volcano recorded 8 hours of extension prior to a rift
72 eruption in 1997 [Owen et. al., 2000]. On the other hand, a network of borehole
73 strainmeters showed transient motion only 30 minutes prior to a basaltic eruption of
74 Hekla in Iceland [Linde et. al., 1993].

75 The large volumes of data provided by modern continuous geodetic networks
76 present both opportunities and challenges. With the order of 10^3 stations, each providing
77 three component positions daily, it is difficult to search for spatially coherent deformation
78 by visual inspection of individual time series. The problem is complicated by the
79 presence of time dependent noise, due to local benchmark motion and unmodeled
80 atmospheric and other effects. Because of this, it is almost certain that more subtle signals,
81 due to smaller magnitude events, exist in data already collected, but have gone
82 undetected. Given the size of the data sets involved and the subtle nature of small
83 transients it is clear that automated detection algorithms would be very desirable.

84 In this paper, we present a new method for detecting spatially and temporally
85 coherent signals in data from large GPS arrays, which is referred to as a Network Strain
86 Filter (NSF). The method builds on previous efforts to develop time dependent methods
87 for inverting geodetic data for slip on faults and dilation of magma bodies, collectively
88 referred to as the Network Inversion Filter (NIF) [Segall and Mathews, 1997; McGuire
89 and Segall, 2003; Fukuda et al, 2004; 2008]. The NIF is a time domain (Kalman) filter
90 that analyzes all data from a network simultaneously, rather than processing individual
91 time series station by station. This allows the NIF to detect spatially coherent transients

92 from the steady-state background strain field. This method has been applied to geodetic
93 data from California [Segall et al., 2000; Murray and Segall, 2005], Taiwan [Hsu et al,
94 2007], Turkey [Bürgmann et al., 2002], Cascadia [McGuire and Segall, 2003], Sumatra
95 [Hsu et al, 2006], and Japan [Aoki et al., 1999; Miyazaki et al., 2003; 2006; Ozawa et al,
96 2001; 2002; 2003; 2005; Miyazaki and Larson, 2008], and successfully imaged aseismic
97 fault slip and magma intrusion.

98 A potential disadvantage of the NIF for detecting strain transients is that it
99 requires one to specify potential sources of deformation, such as faults or magma
100 chambers prior to analysis. While it is possible to develop such models for small areas,
101 doing so for all of Japan or all of western North America is a daunting proposition.
102 Furthermore, if either the model fault geometry or the Green's functions used to relate
103 fault slip to displacement are not fully accurate, the estimate will be biased, and possible
104 transients may be missed. What is needed is a method that identifies spatially coherent
105 transient deformation, but does not require source-specific models. This is the intent of
106 the NSF. In the event that an interesting signal is detected, independent data could be
107 sought to confirm the transient, and more detailed modeling, possibly using the NIF,
108 could be undertaken.

109 In the NSF, GPS time-series data are expressed as a sum of steady site velocities,
110 spatially coherent displacements representing transient crustal deformation, spatially un-
111 correlated benchmark wobble, and reference frame errors. From the displacement time
112 histories it is possible to derive time dependent maps of surface displacement, velocity,
113 and strain-rate, from which it is possible to detect transient deformation. In our approach
114 the deformation terms are expanded in a wavelet basis. While other bases could be

115 employed, wavelets are efficient for representing spatially localized processes and they
116 have proven to be advantageous in estimating deformation fields from GPS data [Tape et
117 al., 2009]. The coefficients of the wavelet basis, along with other time varying quantities
118 are estimated by Kalman filtering, as in the Network Inversion Filter. The approach
119 outlined here handles data from entire networks simultaneously and thus may be able to
120 detect subtle tectonic signals that are difficult to recognize from individual time-series,
121 while at the same time requiring no source-specific parameterization.
122

123 **2. Method**

124 **2.1. Formulation**

125 In this section we present the formulation of NSF for data consisting of time series of
126 station positions from GPS arrays. The extension to time series of EDM, or similar
127 differential displacement measurements is obvious. Point strain and tilt data could also
128 be included in a straightforward manner, but is not done so here.

129 The position $\underline{x}$ at time t is expressed as,

130

131 $$\underline{x}\ (t) = \underline{x}\ (t_0) + \underline{v}\cdot (t - t_0) + \underline{u}(\underline{x},t) + \underline{L}(\underline{x},t - t_0) + \underline{\underline{F}}\,\underline{f}\ (t) + \underline{\varepsilon} \qquad \underline{\varepsilon} \sim N(0,\sigma^2\underline{\underline{\Sigma}}_{\mathbf{x}}) \quad (1)$$

132

133 where $\underline{v}$ represents the secular site velocity, while $\underline{u}(\underline{x},t)$ represents a spatially coherent
134 displacement field. An alternative approach is to expand the steady-state secular
135 displacements in basis functions as with the transient motions, however this approach
136 introduces additional parameters, and complicates transient detection. The transient

displacements $\underline{u}(\underline{x},t)$ include both tectonic and non-tectonic (e.g. fluid withdrawal) components. Unlike the NIF, where the source of deformation is explicitly modeled, the NSF does not attempt to distinguish between tectonic and non-tectonic transients.

The fourth term in (1), $\underline{L}(\underline{x},t-t_0)$, represents site-specific noise from local benchmark instability, which we model as a Brownian random walk with scale parameter τ (units length time$^{-1/2}$) (Wyatt, 1989). For numerical efficiency, we combine the terms $\underline{x}(t_0)$ and $\underline{L}(\underline{x},t-t_0)$, into a single random walk which initiates at $\underline{x}(t_0)$. The term $\underline{\underline{F}}\,\underline{f}\,(t)$, accounts for reference frame errors, where $\underline{\underline{F}}$ is a Helmert transformation, and $\underline{f}\,(t)$ is a vector of rigid body translations, rotations, and a scale factor [e.g., Miyazaki et al., 2003]. The final term, $\underline{\varepsilon}$, represents observation error, which is assumed to be normally distributed with zero mean and covariance $\sigma^2\underline{\underline{\Sigma}}_{\mathbf{x}}$, where $\underline{\underline{\Sigma}}_{\mathbf{x}}$ is the covariance matrix of the GPS positions provided from GPS analyses, and σ^2 is a scale factor to account for unmodeled errors such as those due to mulitpath, or mismodeling of the tropospheric path delays. In the current implementation, τ is assumed to be the same at all GPS stations. Many GPS time series record seasonal signals which are believed to result from a combination of soil moisture, hydrologic, and atmospheric loading, and antenna mis-modeling. We do not explicitly model seasonal errors in this paper, however it should not be difficult to incorporate the approach of Murray and Segall (2005) in which seasonal terms are modeled with an annual sinusoid with slowly varying amplitude.

The transient tectonic displacements $\underline{u}(\underline{x},t)$ are expanded in spatial basis functions $B(\underline{x})$ with time varying coefficients $c(t)$,

$$u_i(\underline{x},t) = \sum_m^M B_{im}(\underline{x}) c_m(t) \qquad (2)$$

where the subscript i indexes displacement component, and M is the number of basis functions. The coefficients $c(t)$ are modeled as stochastic processes. If the deformation is steady in time, the velocities are constant and $\ddot{c}_m$, $m = 1,\ldots,M$, vanishes (the overdot indicates time derivative). For a nearly steady state process, we model the accelerations by a stochastic process with mean zero and variance α^2. In particular, following Segall and Mathews (1997) we assume the transient velocities follow a random walk

$$\dot{c}(t) = \alpha \int_0^t d\omega(t') \qquad (3)$$

where $\omega(t)$ is an independent white noise process $\omega \sim N(0, I)$ and the constant of integration is absorbed into the secular site velocities. The coefficients $c(t)$ are thus given by integrating (3)

$$c(t) = \alpha w(t), \qquad (4)$$

where $w(t)$ is an integrated random walk (e.g., Segall and Mathews, 1997). Combining equations (2) and (4), the tectonic displacement term in (1) can thus be written as

$$u_i(\underline{x},t) = \alpha \sum_m^M B_{im}(\underline{x}) w_m(t). \qquad (5).$$

All of the time-varying quantities, including the coefficients $w(t)$, the random walk estimates, and reference frame corrections are estimated using Kalman filtering techniques (e.g., Brown and Hwang, 1997), as in the NIF. By choosing a non-parametric representation of the coefficients $w(t)$, we allow the data rather than a priori assumptions determine the time-varying nature of the transient deformation. The hyper-parameter α controls the temporal smoothing of the transient displacements, and can be estimated in the filter using an extended Kalman filtering algorithm as discussed in McGuire and Segall (2003). In this work we assume that α is constant in space and time. Fukuda et al. (2004; 2008) present methods for incorporating time-varying α, which does a better job of capturing abrupt transients. Their methods are computationally intensive and are not implemented here, where our principal goal is to identify subtle rather than abrupt transients, however future work could incorporate this filtering approach.

2.2. Choice of Wavelet Functions

In this section we consider the choice of basis functions $B(\underline{x})$. Several commonly used functions, such as Fourier series, are not well suited because they have global support (that is, they are non-zero over the entire domain) and thus require many terms to represent localized deformation due, for example, to volcanic inflation, or buried fault slip. We require basis functions that are suitable for expressing localized deformation in a large geodetic array. Specifically, the functions should have non-zero values only over a localized area. Furthermore, the basis should be differentiable, so that the resulting strain distribution is well defined. Note we exclude surface fault creep in this analysis; generally the location of creeping faults is known a priori. Additionally, the sparse

distribution of most GPS networks is not optimal for detecting fault creep.

While other choices, such as splines or empirical orthogonal functions could be considered, in this study we use wavelet functions as a spatial basis to represent transient deformation, $\underline{u}(\underline{x},t)$. Here we briefly overview some basic properties of wavelets, starting with the one-dimensional case. For geophysical examples, see Addison (2002); Kumar and Foufoula-Gekrgjou (1994); Kumar and Foufoula-Gekrgjou, (1997).

A wavelet $\psi(x)$ is a wave-like function with unit 2-norm $\int |\psi(x)|^2 \, dx = 1$, (e.g., Mallet, 1998). The Deslauriers-Dubuc interpolation wavelet of degree 3 is shown in Figure 1 as an example of one-dimensional wavelet. A family of wavelet functions $\{\psi_{j,k} \mid j,k \in \boldsymbol{Z}\}$ (where $\boldsymbol{Z}$ is the set of integers) can be formed by dilating (or contracting) and translating a unit wavelet ψ, which is sometimes called an analyzing or mother wavelet. One such realization of a discrete, dyadic wavelet family is

$$\psi_{j,k}(x) = 2^{-\frac{j}{2}} \psi\left(\frac{x - k2^j l}{2^j}\right) \quad j,k \in \boldsymbol{Z} \qquad (6).$$

The indices j and k refer to different scales and shifts, respectively, and $l > 0$ is the discretization increment [Kumar and Foufoula-Gekrgjou, 1997].

Orthogonal wavelets, which are orthogonal to all of their translates and dilates (Mallet, 1998), have desirable properties. In particular all square integrable functions $g(x)$ can be represented to arbitrary precision by a linear combination of the form,

$$g(x) = \sum_{j=-\infty}^{\infty} \sum_{k=-\infty}^{\infty} \psi_{j,k}(x) q_{j,k} \qquad (7),$$

where $q_{j,k}$ are coefficients. Note that as the scale gets larger, increasing j, the number of translations, and thus the number of coefficients, decreases.

Orthogonal wavelets typically lack simple closed form expressions in the spatial domain and are defined only on a regular grid. The distribution of GPS stations in the real world, however, is irregularly spaced. Simply calculating the value of an orthogonal wavelet for irregularly spaced points is not as simple as it is for some non-orthogonal wavelets that have closed form expressions. We proceed as follows; orthogonal wavelets are obtained by solving two-scale difference equations that provide values on a dyadic grid [Daubechies, 1992]. By setting the grid spacing to be sufficiently small and using linear interpolation between the grid points, we are able to calculate values at arbitrary points with reasonable precision.

An advantage of orthogonal wavelets is that it enables the introduction of a scaling function (or "father wavelet"), and so-called multi-resolution analysis (MRA). When we introduce a scaling function $\phi(x)$, the terms with higher scales ($j \geq j_0$) in the expansion (7) in terms of the analyzing wavelet can be replaced by a single scaling function (at scale j_0). Namely, with no loss of information, (7) can be written as,

$$g(x) = \sum_{k=-\infty}^{\infty} \phi_{j_0,k}(x) q^s_{j_0,k} + \sum_{j=-\infty}^{j_0} \sum_{k=-\infty}^{\infty} \psi_{j,k}(x) q^a_{j,k} \qquad (8),$$

where

$$\phi_{j,k}(x) = 2^{-\frac{j}{2}} \phi(\frac{x - k2^j l}{2^j}) \quad j,k \in \mathbf{Z} \qquad (9),$$

and $q^s_{j,k}$ and $q^a_{j,k}$ represent the coefficients of the scaling function and analyzing

247 functions for the given scale and translation, respectively. It should be noted that dilates
248 and translates of the scaling function $\{\phi_{j,k} \mid j,k \in Z\}$ also form an orthogonal basis. In
249 (8) all of the terms above the scale j_0 are replaced with a single scaling function (See
250 Appendix A). In practice we represent the displacements with finite sums of the form of
251 equation (8). Choosing $j_0 = 0$, and a minimum wavelet scale j_{min}, then $j = j_{min}, \ldots,-2,-$
252 1,0, and $k = 0, 1, 2, \cdots, 2^{-j_{\min}} - 1$.

253 We examined several wavelets to use as a basis for this analysis. Among wavelets,
254 the "Deslauriers-Dubuc interpolation wavelets" (hereafter referred to as DD wavelet) are
255 advantageous. Though they are not exactly orthogonal, they are suitable for MRA, have
256 compact support and are smooth (Sweldens and Schröder, 1996). DD wavelets of degree
257 $2p$-1 are constructed to have compact support over [-$2p$+1, $2p$-1] (see for example, Mallat,
258 1999; Sweldens and Schröder, 1996). For p=1, the wavelet is a piecewise linear function.
259 When p =2, the wavelet is smoother, with a somewhat Gaussian shape. As p gets larger,
260 the support increases. We have found that the DD wavelet with p=2 (degree 3) is a
261 reasonable compromise between the size of the compact support and the computational
262 burden of calculating the wavelet. The one-dimensional DD wavelet is illustrated in
263 Figure 1.

264 An alternative approach is to use non-orthogonal wavelets, such as the Mexican
265 hat wavelet (second derivative of the Gaussian). The advantage of non-orthogonal
266 wavelets is that they often have explicit analytical forms and are therefore easier to
267 compute. A disadvantage of non-orthogonal wavelets is that they do not have the
268 decomposition (8) and therefore care is needed at the longest spatial scales. While not
269 reported here, we have also conducted numerical experiments with non-orthogonal

wavelets that achieve comparable results to those presented here with the DD orthogonal wavelets. An alternative choice would be to follow the utilization of spherical wavelets by Tape et al., [2009] which could be advantageous for networks with a large spatial extent and has proven successful in estimating static velocity and strain fields from geodetic datasets [Tape et al., 2009]

In this work we analyze only the horizontal displacements, although the method can be simply extended to include the (noisier) vertical component. At present we neglect earth curvature, such that the east and north components of displacement are expressed as functions of Cartesian coordinates, $u_E(x_E,x_N,t)$ and $u_N(x_E,x_N,t)$. We assume a separable isotropic basis, so that two-dimensional wavelets are constructed as tensor products of corresponding one-dimensional wavelets. As explained in Appendix B, the two dimensional representation includes tensor products of: 1) wavelets in the East-direction with wavelets in the North-direction, 2) wavelets in the East-direction with scaling functions in the North-direction, 3) wavelets in the North-direction with scaling functions in the East-direction, and 4) scaling functions in East and North directions. The transient deformation term from equation (5) can thus be expressed as

$$\begin{aligned}\sum_{m}^{M} B_{im}(x_E,x_N)\,w_m(t) = &\sum_{k_1}\sum_{k_2} \Phi^{s}_{j_0,k_1,k_2}(x_E,x_N)\,w^{s}_{j_0,k_1,k_2}(t) \\ &+ \sum_{j=j_{\min}}^{j_0}\sum_{k_1}\sum_{k_2} \Psi^{e}_{j,k_1,k_2}(x_E,x_N)\,w^{e}_{j,k_1,k_2}(t) \\ &+ \sum_{j=j_{\min}}^{j_0}\sum_{k_1}\sum_{k_2} \Psi^{n}_{j,k_1,k_2}(x_E,x_N)\,w^{n}_{j,k_1,k_2}(t) \\ &+ \sum_{j=j_{\min}}^{j_0}\sum_{k_1}\sum_{k_2} \Psi^{d}_{j,k_1,k_2}(x_E,x_N)\,w^{d}_{j,k_1,k_2}(t)\end{aligned} \qquad (10)$$

where j_{min} and j_0 ($j_{min} \le j_0$) are the minimum and maximum scales respectively.

289 $\Phi^s{}_{j_0,k_1,k_2}$ is the two-dimensional scaling function, and $\Psi^e{}_{j,k_1,k_2}$, $\Psi^n{}_{j,k_1,k_2}$, $\Psi^d{}_{j,k_1,k_2}$ are the
290 three two-dimensional analyzing functions (which we refer to as east-west, north-south,
291 and diagonal analyzing wavelets; see Appendix B for details), and $w^s{}_{j_0,k_1,k_2}$, $w^e{}_{j,k_1,k_2}$,
292 $w^n{}_{j,k_1,k_2}$, $w^d{}_{j,k_1,k_2}$ are coefficients. Owing to the property of the MRA, we can set the
293 maximum scale to an arbitrary integer, thus we hereafter set the maximum scale j_0 to be
294 zero; all signals at longer spatial wavelengths are included in the scaling function
295 $\Phi^s{}_{j_0,k_1,k_2}$. Given the periodic (wraparound) condition, where wavelets that spill over at
296 one side of the boundary are wrapped around at the other side, the scaling function, $\Phi^s{}_{j=0}$
297 becomes constant [Addison, 2002]. The three analyzing wavelets are illustrated in Figure
298 2 for the DD wavelet at the scale, j = -1. Note that the number of translations, k_1 and k_2,
299 are functions of the scale j, as they are in the one-dimensional case.
300
301 **2.3. Minimum scale and Regularization**
302 As discussed in the previous section, the number of translations is limited by the
303 extent of geodetic array. Some consideration, however, is needed to choose the minimum
304 and maximum wavelet scales. The largest scale is set by the extent of the geodetic array
305 in latitude and longitude; the analyzing wavelets are contracted to represent smaller scale
306 structures. The choice of minimum scale wavelet is determined by the station spacing.
307 Choosing a minimum scale that is too small results in mapping local noise processes into
308 deformation, leading to spurious estimates of transient deformation. At the extreme,
309 there is no point in including wavelets that do not span any geodetic stations. Even
310 excluding this case, there are generally more wavelet coefficients than there are stations;
311 the problem is strictly under determined.

312 To produce a smooth strain field that satisfies the geodetic observations thus
313 requires some weighting of the wavelet coefficients. We regularize the otherwise
314 underdetermined estimation problem by minimizing a spatial norm of the transient strain-
315 rate field, $\lambda^2 \left\| \dot{\varepsilon}(x) \right\|_S^2$, where $\dot{\varepsilon} = \partial \dot{u} / \partial x$ (for the time being we consider one-dimension
316 only; tensor components are discussed below), the subscript S indicates a smoothing
317 norm, and λ^2 is a scalar. We define a second derivative, smoothing (semi-) norm as
318

319 $$\left\| f(x) \right\|_S^2 = \int_{-\infty}^{\infty} \left(f''(x) \right)^2 dx \qquad (11)$$

320 where prime indicates spatial derivative. Expanding the transient strain-rate field in
321 spatial basis as in (2),
322

323 $$\dot{\varepsilon}(x,t) = \sum_m^M B'_m(x) \dot{c}_m(t) \qquad (12)$$

324

325 the norm of the strain-rate field can thus be written as
326

327 $$\left\| \dot{\varepsilon}(x) \right\|_S^2 = \dot{c}^T \Gamma \dot{c} \qquad (13)$$

328

329 where the components of the Gramm matrix Γ are given by $\Gamma_{ij} = < B'_i, B'_j >$. Here $< , >$
330 indicates the inner product associated with the smoothing norm in (12). It should be
331 noted that because the norm in (13) is a derivative norm, the orthogonality of the
332 wavelets does not imply that the Gramm matrix is the unit matrix, in fact it is not.

Given a wavelet basis of the form (6), the inner products that yield the components of the Gramm matrix are of the form

$$
\begin{aligned}
&< \frac{\partial \psi_{j,k}}{\partial x}, \frac{\partial \psi_{m,n}}{\partial x} >=< 2^{-j/2} \frac{\partial \psi}{\partial x}(\frac{x}{2^j} - kl), 2^{-m/2} \frac{\partial \psi}{\partial x}(\frac{x}{2^m} - nl) > \\
&= 2^{-(j+m)/2} < \frac{\partial \psi}{\partial x}(\frac{x}{2^j} - kl), \frac{\partial \psi}{\partial x}(\frac{x}{2^m} - nl) > .
\end{aligned}
\tag{14}
$$

For general j,m, and k,n the resultant inner product may have to be integrated numerically. Note however, that because wavelets have compact support, the inner product will vanish for wavelets of the same scale ($j = m$) and offset greater than the wavelet's support.

To the extent possible given the data, a smooth solution maps the signal into the longer wavelength spatial scales. Thus, of particular interest is the contribution to the Gramm matrix from wavelets at the same offset but different scales. This determines how the different spatial scales should be weighted in the estimation. For $j = m$, $k = n$, and the second difference semi-norm (11), equation (14) becomes

$$
< \frac{\partial \psi_{j,k}}{\partial x}, \frac{\partial \psi_{j,k}}{\partial x} >= 2^{-j} \int_{-\infty}^{\infty} \left(\frac{\partial^3 \psi}{\partial x^3}(\frac{x}{2^j} - kl) \right)^2 d\xi
\tag{15}
$$

Making the substitution $\xi = 2^{-j} x - k L$ and applying the chain-rule yields,

$$< \frac{\partial \psi_{j,k}}{\partial x}, \frac{\partial \psi_{j,k}}{\partial x} >= 2^{-6j} \left\| \psi'(\xi) \right\|^2 = 2^{-6j} \int_{-\infty}^{\infty} \left(\psi'''(\xi) \right)^2 d\xi \qquad (16)$$

Equation (16) shows that weighting the different wavelet scales by 2^{-6j} is appropriate given the specified smoothing norm and associated inner product. The integral in (16) represents the squared norm of the gradient of the mother wavelet. The Gramm matrix also includes terms related to the inner product of wavelets at different scales and offsets. For the current study we have not computed the full Gramm matrix, rather approximating it with a diagonal matrix with entries of the form (16). With this approximation, it is not actually necessary to compute the integral in (16), as this value can be absorbed into the scalar λ^2.

In two dimensions we employ a Laplacian (semi) norm

$$\left\| f(x,y) \right\|_S^2 = \int_{-\infty}^{\infty} \int_{-\infty}^{\infty} \left(\nabla^2 f(x,y) \right)^2 dx dy \,, \qquad (17)$$

In 2D each velocity component is expanded in four sets of sums, as in equation (10). However, due to the distributive property of the inner product, this simply results in (many) more terms in the computation of each entry in the Gramm matrix. Also, as discussed in Appendix B we form 2D wavelets as tensor products of one-dimensional wavelets. Importantly, the norm of any component of the strain-rate, or any linear combination of strain-rate components such as the areal dilatation rate, will involve (partial) derivatives of order three – one from the definition of strain and two from the second derivative smoothing. Thus, the norm of any of the surface strain-rate components

at the same scale and offset scales with 2^{-6j} as in 1D. In contrast, first derivative smoothing of the strain-rate field scales with 2^{-4j}. Our numerical tests indicate better results with second derivative smoothing, so that is employed here. With a diagonal approximation of the Gramm matrix, the definite integrals of the mother wavelets and scaling functions can be absorbed into the smoothing parameter λ^2, as in the one-dimensional case. While one presumable achieves better results by numerically computing the full Gramm matrix, we have not attempted to do so.

2.4. Kalman Filtering

The unknowns to be estimated at each observation epoch include the secular velocity at each station, the coefficients representing the transient displacement field, the random walk benchmark components, the reference frame parameters, and the temporal smoothing hyper-parameter (α). All of these are incorporated into the state vector **X** that is estimated by the extended Kalman filter (Appendix C). The total number of parameters estimated at each epoch is 4*M (M=number of basis functions, times 2 components of displacement, times 2 coefficients/basis) + 2*N (for the secular velocity of each component) + 2*N (for benchmark wobble at each station) + 2 (reference frame translations in each component) + 1 (the hyper parameter α). The total number of basis functions M is 1 (for the scaling function) + 3*(Number of scales; $j_0 - j_{min} + 1$)*(Number of wavelet translations at each scale (for Ψ^e, Ψ^n, and Ψ^d)). However, in practice, we do not include basis functions that are poorly observed by a particular network in the estimation. For the studies shown below, we have only included basis functions which

397 have an amplitude of ≥ 10% of the peak amplitude at ≥ 5 stations. Tape et al. (2009)
398 followed a similar selection approach in estimating continuous velocity fields from
399 discrete data using wavelet basis functions.

400 The state vector at all epochs is estimated through an extended Kalman filter, a
401 recursive least squares estimator. The state at epoch k, given data up to that epoch is
402 written as $\underline{X}_{k|k}$, with covariance matrix $\underline{\underline{C}}_{k|k}$. The state at epoch k+1 is predicted based on
403 the stochastic state evolution equations yielding, $\underline{X}_{k+1|k}$. New data at epoch k+1 is
404 incorporated in a weighted least-squares sense, leading to an updated state. This state is
405 conditional on data up to epoch k+1, written as $\underline{X}_{k+1|k+1}$ with covariance $\underline{\underline{C}}_{k+1|k+1}$. These
406 estimates, based on all available data up to the current epoch, are referred to as filtered
407 estimates. The process iterates until the final data epoch; if there are N_e epochs, this
408 yields $\underline{X}_{N_e|N_e}$. Smoothed estimates, conditional on all data, $\underline{X}_{k|N_e}$, are obtained by
409 backward application of the Kalman filter (see Appendix C).
410
411 Following Segall and Matthews (1997) the regularization is introduced in the
412 Kalman filter through the a priori state $\underline{X}_{1|0}$ and covariance, $\underline{\underline{C}}_{1|0}$, that is the state prior to
413 the first observations [see Segall and Matthews, 1997; equation 50]. For the transient
414 velocity coefficients, the $\dot{c}$ terms in equation (3), we set the prior state to zero, and the
415 corresponding components of the prior covariance matrix to $\underline{\underline{C}}_{1|0} = \frac{1}{\lambda^2} diag(2^{6j})$, where
416 *diag* indicates a diagonal matrix. That is, all wavelet coefficients are a priori set to zero,
417 but that the confidence in this is least for the longest wavelength spatial scales. Thus, the
418 coefficients only move away from zero if the data demand. The coefficients

corresponding to the transient *displacement* on the other hand are set to zero, with very small variance, 1e-8 m^2, because at time $t = 0$, there has been no time for transient displacement to accumulate. The secular site velocities are also initialized at zero, but with very broad prior uncertainty (0.05 m/yr). For the reference frame terms the $\underline{\underline{C}}_{1|0}$ terms are set to 1e-4 m^2, which is sufficient in our experience to absorb frame errors in actual data sets. For the random benchmark motion term, we set $\underline{\underline{C}}_{1|0}$ terms to 1e-4 m^2, which as explained above accounts for uncertainty in the site position at the initial epoch. For the synthetic tests conducted here the random walk error is taken to be 3 $mm/yr^{1/2}$.

The prior estimate and variance of the temporal smoothing parameter α requires some consideration. In our experience a poor choice of α can lead to instability in the extended Kalman filter. Our implementation actually propagates $\log(\alpha)$, which has the benefit of keeping this quantity non-negative. In the simulations here we initialize the filter with a a small value, e.g, $\log(\alpha)_{1|0}$=-9 with large variance $\mathrm{Var}[\log(\alpha)]_{1|0}$=7. This allows sufficient leeway for the temporal smoothing parameter to adapt to transients. In practice for a given dataset, the prior value of α has to be adjusted so that it implies a nearly steady transient field, such that any actual transients will force the estimate of α to increase [McGuire and Segall, 2003].

As a check on the filtered estimates the residual variance should be consistent with that expected given nominal errors in the data. From equation (1) the predicted data is given by

$$\hat{\underline{x}}(t) = \hat{\underline{x}}\ (t_0) + \hat{\underline{v}} \cdot (t - t_0) + \hat{\underline{u}}(\underline{x}, t)\ + \underline{\underline{F}}\,\hat{\underline{f}}\ (t) \qquad (18)$$

where the hat indicates predicted value. Thus, the residual variance in the station positions should be

$$\mathrm{var}(\underline{x}(t) - \hat{\underline{x}}(t)) \sim \mathrm{var}\{(\underline{L}(\underline{x},t) + \underline{\varepsilon})^{apriori}\} = \tau^2(t - t_0) + \sigma^2 \underline{\underline{\Sigma}}_x \qquad (19)$$

since the benchmark motions and white noise are assumed uncorrelated. One can check the filter residuals to ensure that this is reasonably well satisfied. It should be noted however that residuals satisfying (19) does not prove that the filter has correctly resolved the signal into its constituent components, transient displacement, random walk, reference frame error, etc. The various components of the state vector must be examined a posteriori to demonstrate consistency with the model assumptions.

3. Synthetic Test

We carried out simulations to test the performance of the filter by analyzing synthetic GPS data. We generated synthetic data for a network with the geometry of the South California Integrated GPS Network (SCIGN) with 219 stations. We set a hypothetical buried fault, 250 km long and 20 km wide, with a dip of 10 degrees running along the strike of the San Andreas Fault. This was not chosen to represent a known structure, but rather to simply generate a coherent transient field. We generated a six year long synthetic time series, with a slow slip event starting in year two and lasting for three years that produced a transient displacement field concentrated in the L.A. basin (Figure

464 3). The signal amplitude was chosen such that the peak amplitude of the transient field is
465 similar to the amplitude of the benchmark wobble, but both are much smaller than the
466 secular field (Figure 3). The time history of slip is imposed such that resultant
467 displacement has a gradual (slow) initialization, followed by rapid growth, and ends
468 gently. The station displacements are computed from the transient slip using Green's
469 functions for a homogeneous elastic half-space. Secular motion is added based on actual
470 SCIGN data. Finally, we add local benchmark motion, modeled as a random walk process
471 with a scale parameter of 1.5 mm/yr$^{1/2}$, and measurement errors, assumed to be Gaussian
472 white noise with a scale of 2 mm. Due to the long duration of the event, the contributions
473 from secular motion and benchmark wobble make it difficult to identify the transient
474 signal by eye in individual records

475 Figure 4 illustrates the locations and dimensions of the wavelets used to represent
476 the transient deformation field. Note both that there are many more wavelets at the
477 smallest scale, and that the number of small scale wavelets depends on the station density.

478 The primary decision to be made in analyzing the synthetic dataset is the choice
479 of the prior covariance matrix for the state vector. We follow the procedure as described
480 in section 2 which is straight-forward for the elements corresponding to the transient
481 displacement, the secular velocity, the benchmark wobble, and the frame translations.
482 For α, we chose a prior ($\log(\alpha)_{1|0} = -9$; $\mathrm{Var}[\log(\alpha)]_{1|0}=7$) that corresponds to the *a priori*
483 assumption that there are no significant transient displacements, but allows the freedom
484 for the estimate of α to increase if required by the data. To estimate λ^2, we ran the filter
485 for a number of values of λ^2 and calculated the model norm of the resulting transient
486 strain field (eq 13, but with $\boldsymbol{c}$ rather than its time derivative) at the final epoch. The

487 tradeoff between the roughness of the transient field and the magnitude of λ^2 is very
488 strong (Figure 5). This tradeoff arises because small values of λ^2 allow the secular field
489 to be mapped into the transient field. In the limit that λ^2 is extremely small, there is no
490 need for the elements of the state vector corresponding to the secular field, because the
491 entire signal can be mapped into an arbitrarily rough transient field. This can be seen in
492 the temporal evolution of the filtered estimate of α for different values of λ^2 (Figure 6).
493 For small values of λ^2 (say 0.001) the filter maps the (large amplitude) secular signal into
494 the transient field (because it has larger *a priori* uncertainty), which in turn forces α to
495 increase rapidly (Figure 6). In contrast, when λ^2 is larger α tends to drift toward lower
496 values (consistent with steady deformation) until soon after the onset of the transient
497 (roughly epoch 75 in this example). Our synthetic experiments have indicated that
498 choosing a value of λ^2 that is at or slightly larger than the inflection point in the tradeoff
499 curve (Figure 5) leads to a good recovery of the true transient signal. Figure 7 compares
500 the estimated transient displacement field at the final epoch for two values of λ^2 that
501 bracket the inflection point in the tradeoff curve. Below the inflection point (λ^2=0.05) the
502 recovered signal is a combination of the secular and transient fields, while at the
503 inflection point (λ^2=0.1) the filter has properly separated the transient field from the
504 secular field (Figure 7).

505 The filter's success in identifying the transient for λ^2=0.1 results from the spatial
506 coherence of the transient signal. Through the update equations of the Kalman filter,
507 when the transient displacement begins to increase strongly around the middle of the
508 dataset (~2003.0 in Figure 8, epoch ~75 in Figure 6) the growing residual between the
509 current estimate of the state vector and the data gets mapped into an increase in α, and

hence into an increase in the magnitude of the estimated transient signal. This behavior is very similar to that seen in the NIF employing both synthetic and real datasets (*McGuire and Segall*, 2003). Figure 8 shows examples of the estimated transient (black curves) and benchmark motion terms (green curves) for a station in the middle of the transient region (BRAN, white triangle in Figure 3) and a station far removed from the transient (BILL, southeastern white triangle in Figure 3). The simulated data in Figure 8 has had the estimated secular velocity removed from each component so the sum of the transient field and the benchmark term (shown by the red curve) is effectively a measure of the fit to the data. Both stations have drifts of ~5mm over time periods of a few years due to the benchmark wobble term. For station BILL, the filter properly maps this motion into the benchmark term (green curve) rather than the transient term because this motion is not spatially coherent. For station BRAN, the ~5mm transient motion to the southwest is properly mapped into the estimated transient field because it is spatially coherent with nearby stations (Figure 3). The success of the filter in this case is encouraging given that the amplitude of the signal (~5mm) was similar to that of the colored noise at a given station, given the long duration of the simulated transient.

4. Application to the 1996 Boso slow earthquake

In May, 1996, anomalous transient displacements were observed in the Japanese continuous GPS array, GEONET, deployed by the Geographical Survey Institute (GSI) of Japan (Ozawa et al., 2003; Sagiya et al, 2004). Similar slow slip events were also observed in 2002 and 2007 (Ozawa et al., 2007). The stations exhibiting transient motion cover the whole Boso peninsula, extending about a 100 km by 100 km area (Figure 9). The time series in and around the Boso peninsula clearly shows that the GPS stations

exhibit gradual movement toward the southeast, with amplitudes of up to ~10 mm and a duration of about 10 days. The amplitude decreases with distance from the station CHIO (the southeast station in Figure 9) suggesting that the source is located offshore of CHIO. Several studies concluded that this transient deformation resulted from aseismic slip on the interface between the subducting Pacific plate and the overlying plate (Ozawa et al., 2003; Sagiya et al., 2004).

We used GPS data around the Boso peninsula recorded by GEONET to test the capability of the NSF for automated detection of this transient. We used 47 GPS stations (Figure 9), with 104 daily position determinations from April 1 to July 13 in 1996, including approximately 40 days before and after the transient event. The daily station coordinates are those obtained through routine analysis of the Geographical Survey Institute of Japan (Hatanaka, 2003; Geographical Survey Institute, 2004). Routine GEONET analysis divides the network into regional subnetworks; stations around the Boso peninsula belong to the "south Kanto-Tokai district" that consist of the same antenna-receiver-monument type. This avoids errors due different antenna phase center variations. Here, we chose stations around the south Kanto district, excluding the more distant stations in the Tokai district.

We applied the NSF to the GEONET data using the same procedure as for the simulation. Because of the relatively small area, we only consider the translational components in the reference frame errors. For this relatively short data set, neither secular displacements nor seasonal variations are significant. The DD wavelet function of the degree 3 is employed as a basis, and only horizontal components of the time series are analyzed.

556 We determined an appropriate value of the spatial smoothing parameter λ^2
557 following the same method as in the synthetic test. The tradeoff curve (Figure 10) is
558 similar to the synthetic example (Figure 5) and we choose $\lambda^2=2$ as the best estimate. The
559 abrupt nature of this transient results in a very clear increase in the temporal smoothing
560 parameter α at epoch 45 for all values of λ^2 (Figure 11). Owing to the short duration of
561 the dataset, we set the prior variance on the secular term to be very small (25 $(mm/yr)^2$)
562 since this would not be well resolved. The scale factors, σ and τ, were set to 5 and 10
563 $mm/\sqrt{year}$, based on inspection of the time series. The minimum scale of -2 was
564 determined to be sufficient to represent the transient field for this relatively small array.
565 The time history of the estimated transient signal is illustrated in Figure 12 for
566 several stations. The variation in the amplitude of the inferred transient signal from
567 station to station is consistent with the data. However the transient is stretched out over a
568 longer time period from roughly 1996.33 to 1996.40 than the data. The estimated
569 transient field in Figure 12 begins before the actual transient due to the backsmoothing
570 process in the filter algorithm. The signal is oversmoothed in the time-domain because
571 one value of α is assumed to apply to the entire dataset which is transient free for the first
572 and last 40 epochs. Clearly an implementation that allows for a time variable α, such as
573 the particle filter approach used by *Fukuda et al*. [2004], would be necessary to
574 accurately recover the abrupt time history of the transient. However, for the purpose of
575 detecting the transient, the ~1 week error bias in oversmoothing is not a significant
576 drawback. Overall the transient is well localized in both space (Figure 9) and time
577 (Figure 12), demonstrating the ability of the NSF to find such events in real datasets.

5. Discussion

Results presented in the previous sections show that a combination of wavelets with Kalman filtering techniques enables us to separate spatially coherent transient signals from secular motions and localized, colored noise processes, without introducing source-specific models. An important application of the NSF is to search for subtle signals due to smaller slow earthquakes, which would be useful in systematic mapping of slow earthquakes or similar processes in tectonic regions such as Japan, Cascadia and California. The algorithm is capable of detecting subtle coherent motions that would be good candidates for further analysis. For example, regions the NSF identified as hosting possible transients could be analyzed using the fault-based Network Inversion Filter. Like the NIF, the NSF takes advantage of information from the whole network simultaneously. This should be superior to methods that treat individual time series separately and subsequently search for spatial coherence. Additionally, all of the parameters including secular velocity are estimated simultaneously rather than having to be removed ahead of time which may introduce spurious transients.

As seen in the recovered transient time series, for both the simulations and the Boso Peninsula data, there is a tendency for the filter to produce overly smooth estimates of the transient signal. This is a well-known attribute of the stochastic model, which assumes small departures from steady-state, equation (3), with a constant temporal smoothing parameter (see discussion in Segall and Matthews, 1997). Fukuda et al. (2004; 2008) have introduced a Monte Carlo Mixture filter that propagates a discrete representation of the probability density function of α, rather than its mean and covariance. Furthermore, α is allowed to evolve based on variations in the data. Such an

601 approach, coupled to the expansion in equation (5), would allow for improved recovery
602 of the transient displacement field.
603
604
605 **Acknowledgments.** We thank L. Zhen for producing the synthetic GPS data used
606 in simulations, the Geographical Survey Institute of Japan for the GPS data access, and A.
607 Morimoto for useful information about wavelets. We thanks for the Grant-in-Aid for
608 Young Scientists [KAKENHI(18740283)] of the Minnistry of Education, Culture, Sports,
609 Science and Technology and the postdoctoral fellowships for research abroad of the
610 Japan Society for the Promotion of Science. We also acknowledge NASA and SCEC.
611 This research was supported by the Southern California Earthquake Center. SCEC is
612 funded by NSF Cooperative Agreement EAR-0106924 and USGS Cooperative
613 Agreement 02HQAG0008. The SCEC contribution number for this paper is ####. We
614 used the Wavelab package to calculate wavelets. R.O. is grateful for continuous support
615 from the members of the tectono-hydrology research team of the Geological Survey of
616 Japan.
617
618

619 **References**

620 Addison, P., *The Illustrated Wavelet Transform Handbook: Introductory Theory and*
621 *Applications in Science, Engineering, Medicine and Finance*, 353 pp, Institute of
622 Physics, London, 2002.

623 Aoki, Y., P. Segall, T. Kato, P. Cervelli, and S. Shimada., Upward dike migration during
624 the 1997 seismic swarm off the Izu Peninsula, Japan, from inversion of deformation
625 data, *Science, 286*, 927-930, 1999.
626 Brooks, B. A., Foster, J.H., Bevis, M., Frazer, L. N., Wolfe, C. J., and Behn, M., Periodic
627 slow earthquakes on the flank of Kilauea volcano, Hawai´I Earth and Planetary
628 Science Letters, Volume 246, Issue 3-4, p. 207-216, 2006.
629 Brown and Hwang, *Introduction to Random Signals and Applied Kalman Filtering*, 496
630 pp, John Wiley & Sons, Inc., 1996.
631 Brudzinski M R, and R M. Allen, Segmentation in episodic tremor and slip all along
632 Cascadia, Geology v. 35, 907-910, 2007.
633 Bürgmann, R., S. Ergintav, P. Segall, E. Hearn, S. McClusky, R. E. Reilinger, H. Woith,
634 and J. Zschau, Time-dependent distributed afterslip on and deep below the Izmit
635 earthquake rupture, *Bull. Seis. Am., 92*, 126-137, 2002.
636 Cervelli, P., P. Segall, K. Johnson, M. Lisowski, and A. Miklius, Sudden aseismic fault
637 slip on the south flank of Kilauea volcano, *Nature*, 415, 1014 – 1018, 2002.
638 Daubechies, I., *Ten Lectures on Wavelets*, CBMS-NSF Regional Conference Series in
639 *Applied Mathematics*, 377 pp., Soc. for Ind. and Appl. Math., Philadelphia, PA., 1992.
640 Delahaye, E. J., J. Townend, Reyners and G. Rogers, Microseismicity but no tremor
641 accompanying slow slip in the Hikurangi subduction zone, New Zealand, *EPSL*, 277,
642 2009.
643 Douglas,A., J Beavan, L Wallace, J Townend, Slow slip on the northern Hikurangi
644 subduction interface, New Zealand *Geophys. Res. Lett,* 2005.

645 Dragert, H., K. Wang, and T. S. James, A silent slip event on t he deeper Cascadi a
646 subduct i on i nt erface, *Science*, 292, 1525 – 1528, 2001.
647 Fukuda, J., T. Higuchi, S. Miyazaki, and T. Kato, A new approach to time-dependent
648 inversion of geodetic data using a Monte Carlo mixture Kalman filter, *Geophys. J. Int.,*
649 159, 17-39, 2004.
650 Fukuda, J., Miyazaki, S, Higuchi,T., and T. Kato, Geodetic inversion for space–time
651 distribution of fault slip with time-varying smoothing regularization, *Geophys. J. Int.,*
652 173, 25-48, 2008.
653 Geographical Survey Institute, Establishment of the nationwide observation system of
654 1,200 GPS-based control stations, *Bull. Geogr. Surv. Inst.*, 3–51, 103, 2004 (in
655 Japanese).
656 Hatanaka, Y., T. Iizuka, M. Sawada, A. Yamagiwa, Y. Kikuta, J. M. Johnson, and C.
657 Rocken, Improvement of the analysis strategy of GEONET, *Bull. Geogr. Surv. Inst.*,
658 **49**, 11–37, 2003.
659 Heki, K., S. Miyazaki, and H. Tsuji, Silent fault slip following an interplate thrust
660 earthquake at the Japan Trench, *Nature*, 386, 595 – 598, 1997.
661 Hirose, H., and K. Obara, Repeating short- and long-term slow slip events with deep
662 tremor activity around the Bungo Channel region, southwest Japan, *Earth Planets*
663 *Space*, 57, 961 – 972, 2005.
664 Hirose, H., and K. Obara, Short-term slow slip and correlated tremor episodes in the
665 Tokai region, central Japan, *Geophys. Res. Lett.*, 33, L17311,
666 doi:10.1029/2006GL026579, 2006.

667 Hirose, H., K. Hirahara, F. Kimata, N. Fujii, and S. Miyazaki, A slow thrust slip event
668 following the two 1996 Hyuganada earthquakes beneath the Bungo Channel,
669 southwest Japan, *Geophys. Res. Lett.*, 26, 3237 – 3240, 1999.
670 Hsu, Y.-J., P. Segall, S.-B. Yu., L.-C. Kuo, and C. A. Williams, Temporal and spatial
671 variations of post-seismic deformation following the 1999 Chi-Chi, Taiwan earthquake,
672 *Geophys. J. Int.* 169, doi:10.1111/j.1365-246X.2006.03310.x, 2007.
673 Hsu, Y. J., M. Simons, et al., Frictional afterslip following the 2005 Nias-Simeulue
674 earthquake, Sumatra, *Science*, 312(5782), 1921-1926, 2006.
675 Hudnut, K.W., Y. Bock, J.E. Galetzka, F.H. Webb, and W.H. Young, The Southern
676 California Integrated GPS Network (SCIGN), in *Seismotectonics in Convergent Plate*
677 *Boundary*, Y. Fujinawa and A. Yoshida (Eds.), TERRAPUB, Tokyo, Japan, 167-189,
678 2002.
679 Jackson, D.D., Shen, Z.K., Potter, D., Ge, X.B., and Sung, L.Y., Southern California
680 deformation, *Science*, 277, 1621-1622, doi: 10.1126/science.277.5332.1621, 1997.
681 Kostoglodov, V., S. K. Singh, J. A. Santiago, K. M. Larson, A. R. Lowry and R. Bilham,
682 A large silent earthquake in the Guerrero seismic gap, Mexico, *Geophys. Res. Lett.*, 30,
683 1807, doi:10.1029/2003GL017219, 2003.
684 Kumar, P., and E. Foufoula-Georgiou, Wavelet analysis in geophysics: An introduction,
685 in *Wavelets in Geophysics*, edited by E. Foufoula-Georgiou and P. Kumar, pp. 1-43,
686 Academic, San Diego, Calif., 1994
687 Kumar, P., and E. Foufoula-Georgiou, Wavelet analysis for geophysical applications,
688 *Rev. Geophys*, 385-412, 35, 1997.

689 Larson, K.M., V Kostoglodov, S. Miyazaki, J. A. Santiago, The 2006 aseismic slow slip
690 event in Guerrero, Mexico: New results from GPS, *Geophys. Res. Lett.*, 34, L13309,
691 2007.
692 Linde, A. T., K. Ágústsson, I. S. Sacks and R. Stefánsson, Mechanism of the 1991
693 eruption of Hekla from continuous borhole strain monitoring, *Nature*, 365, 737-740,
694 1993.
695 Linde, A. T., M. Gladwin, M. Johnston, R. Gwyther, and R. Bilham, A slow earthquake
696 sequence on the San Andreas Fault, *Nature*, 383, 65 – 68, 1996.
697 Lowry, A. R., K. M. Larson, V. Kostoglodov, and R. Bilham, Transient fault slip in
698 Guerrero, southern Mexico, *Geophys. Res. Lett.*, 28, 3753–3756, 2001.
699 Mallet, S., *A wavelet tour of signal processing*, *2nd edition*, Academic Press, pp.637,
700 1998.
701 McCaffrey, R., L M. Wallace, J Beavan, Slow slip and frictional transition at low
702 temperature at the Hikurangi subduction zone, *Nature Geoscience*, 1, 316 – 320, 2008.
703 McGuire, J. J., and P. Segall, Imaging of aseismic fault slip transients recorded by dense
704 geodetic networks, *Geophys. J. Int.*, 155, 778 – 788, 2003.
705 Miller, M. M., T. Melbourne, D. J. Johnson, and W. Q. Sumner, Periodic slow
706 earthquakes from the Cascadia subduction zone, *Science,* 295, 2423,
707 doi:10.1126/science.1071193, 2002.
708 Miyazaki, S., J. J. McGuire, and P. Segall, A transient subduction zone slip episode in
709 southwest Japan observed by the nationwide GPS array, *J. Geophys. Res.*, 108(B2),
710 2087, doi:10.1029/2001JB000456, 2003.

711 Miyazaki, S., P. Segall, J. J. McGuire, T. Kato, and Y. Hatanaka, Spatial and temporal
712 evolution of stress and slip rate during the 2000 Tokai slow earthquake, *J. Geophys.*
713 *Res.*, 111, B03409, doi:10.1029/2004JB003426, 2006.
714 Miyazaki, S., and K. Larson, Coseismic and early postseismic slip for the 2003 Tokachi-
715 oki earthquake sequence inferred from GPS data, Geophys. Res. Lett., VOL. 35,
716 L04302, doi:10.1029/2007GL032309, 2008.
717 Murray, J. R., and P. Segall, Spatiotemporal evolution of a transient slip event on the San
718 Andreas Fault near Parkfield, California, *J. Geophys. Res.*, 110, B09407,
719 doi:10.1029/2005JB003651, 2005.
720 Niemi, N., B. Wernicke, A. Friedrich, M. Simons, R. Bennett, and J. Davis, BARGEN
721 continuous GPS data across the eastern Basin and Range province, and implications
722 for fault system dynamics, *Geophys. J. Int.*, 159, 842 – 862, 2004.
723 Norabuena, E., et al., Geodetic and seismic constraints on some seismogenic zone
724 processes in Costa Rica, *J. Geophys. Res.*, 109, B11403, doi:10.1029/2003JB002931,
725 2004.
726 Obara, K, Nonvolcanic deep tremor associated with subduction in southwest Japan,
727 *Science*, 296, 1679 – 1681, 2002.
728 Owen, S., P. Segall, M. Lisowski, A. Miklius, R. Denlinger, M. Sako, Rapid deformation
729 of Kilauea volcano: GPS measurements between 1990 and 1996, *J. Geophys. Res., 105*,
730 18,983-18,998, 2000.
731 Ozawa, S., M. Murakami, and T. Tada, Time-dependent inversion study of the slow
732 thrust event in the Nankai Trough subduction zone, southwestern Japan, *J. Geophys.*
733 *Res.*, 106, 787 – 802, 2001.

734 Ozawa, S., M. Murakami, M. Kaidzu, T. Tada, Y. Hatanaka, H. Yarai, and T. Nishimura,
735 Detection and monitoring of ongoing aseismic slip in the Tokai region, central Japan,
736 *Science*, 298, 1009 – 1012, 2002.
737 Ozawa, S., S. Miyazaki, Y. Hatanaka, T. Imakiire, M. Kaidzu, and M. Murakami,
738 Characteristic silent earthquakes in the eastern part of the Boso peninsula, Central
739 Japan, *Geophys. Res. Lett.*, **30**, 1283, doi:10.1029/2002GL016665, 2003.
740 Ozawa, S., M. Murakami, et al., Transient crustal deformation in Tokai region, central
741 Japan, until May 2004, *Earth, Planets, and Space*, 57, 909-915, 2005.
742 Ozawa, S., Suito H., and Tobita, M., 2007, Occurrence of quasi-periodic slow-slip off
743 the east coast of the Boso peninsula, Central Japan, *Earth Planets Space*, **59**, 1241-
744 1245.
745 Pritchard, M. E., and M. Simons, An aseismic slip pulse in northern Chile and along-
746 strike variations in seismogenic behavior, *J. Geophys. Res.*, 111, B08405,
747 doi:10.1029/2006JB004258, 2006.
748 Rauch, H. E., Tung, F., and Striebel, C. T., 1965, Maximum likelihood estimates of
749 linear dynamic systems, *AIAA J.*, 3, 1445-1450.
750 Rogers, G., and H. Dragert, Episodic tremor and slip on the Cascadia subduction zone:
751 The chatter of silent slip, Science, 300, 1942 – 1943. Sumatra-Andaman earthquake,
752 *Nature*, 440, 46 – 51, 2003.
753 Sagiya, T., Interplate coupling in the Kanto District, central Japan, and the Boso Silent
754 earthquake in May 1996, 2327-2342, 161, *PAGEOPH*, 2004.

755 Sagiya, T., A decade of GEONET: 1994-2003—The continuous GPS observation in
756 Japan and its impact on earthquake studies—, *Earth Planets Space*, 56, pp. xxix-xli,
757 2004.
758 Schwartz, S., and J. Rokosky, Slow slip events and seismic tremor at circum-Pacific
759 subduction zones, *Reviews of Geophysics,* 45 , 2007.
760 Segall, P. and M. Matthews, Time dependent inversion of geodetic data, *J. Geophys. Res.,*
761 *102*, 22,391-409, 1997.
762 Segall, P., R. Bürgmann, and M. Matthews, Time-dependent triggered afterslip following
763 the 1989 Loma-Prieta earthquake, *J. Geophys. Res., 105*, 5,615-5,634, 2000.
764 Segall, P. and J.L. Davis, GPS applications for geodynamics and earthquake studies,
765 *Annual Reviews of Earth and Planetary Science, 25*, 301-36, 1997.
766 Segall, P., E. K. Desmarais, D. Shelly, A. Miklius, and P. Cervelli, Earthquakes
767 Triggered by Silent Slip Events on Kilauea Volcano, Hawaii, *Nature,* 442, 71-74,
768 doi:10.1038/nature04938, 2006.
769 Shelly, David R., Gregory C. Beroza, and S. Ide, Non-volcanic tremor and low-
770 frequency earthquake swarms, *Nature*, 446, 305-307, 2007.
771 Sweldens, S. and P. Schröder, Building Your Own Wavelets At
772 Home,http://www.multires.caltech.edu/teaching/courses/waveletcourse/, 1996.
773 Szeliga, W., Melbourne, T., Santillan, M., Miller, M. GPS constraints on 34 slow slip
774 events within the Cascadia subduction zone, 1997–2005, *J. Geophys. Res.,* 113, 2008.
775 Tape, C., P. Muse, M. Simons, D. Dong, and F. Webb, Multiscale estimation of GPS
776 velocity fields, *Geophys. J. Intl.,* 179, 945-971, 2009.

Wang K., H. Dragert, H. Kao, E. Roeloffs, Characterizing an "uncharacteristic" ETS event in northern Cascadia, *Geophys. Res. Lett.*, 35, L15303, doi:10.1029/2008GL034415, 2008.

Wyatt, F. K., Displacement of surface monuments; vertical motion, *J. Geophys. Res.,* 94, 1655-1664, 1989.

Zhang, J., Y. Bock, H. Johnson, P. Fang, S. Williams, J. Genrich, S. Wdowinski, and J. Behr, Southern California Permanent GPS Geodetic Array: Error analysis of daily position estimates and site velocities, *J. Geophys. Res.*, *102*(B8), 18,035–18,055, 1997.

795

796

797

Appendix A: Multi-resolution Analysis

With a multi-resolution analysis (MRA) the space of all square integrable functions in *p*-dimensions, $L^2(\Re^p)$, is subdivided into nested subspaces spanned by a set of scaling functions (see Mallet, 1988). Define the subspace of $L^2(\Re^p)$ spanned by a family of a scaling functions at a given scale j as

(A1) $$V_j = \overline{\underset{\vec{k}}{\text{Span}}\{\phi_{j,\vec{k}}(\vec{x})\}} \quad \vec{k} = (k_1, k_2, \cdots k_p) \quad k_i \in \boldsymbol{Z}$$

where the over bar denotes closure and $\boldsymbol{Z}$ is the set of integers (Figure A1). In short, V_j represents the subspace spanned by all the translations of the scaling function at scale *j*. MRA requires that the subspaces are nested,

(A2) $$V_j \subset V_{j-1} \quad j \in \boldsymbol{Z}$$

with

(A3) $$V_\infty = \{0\}, \quad V_{-\infty} = L^2(\Re^p).$$

The subspace spanned by wavelets (analyzing wavelets) at scale *j*, W_j is such that

(A4) $$V_{j-1} = V_j \oplus W_j.$$

In other words, the space spanned by the scaling functions at scale *j-1*, is the sum of the subspace spanned by the scaling function and analyzing wavelets at scale *j* (Figure A1). This result readily extends to

(A5) $$V_{j-2} = V_j \oplus W_j \oplus W_{j-1}.$$

It is easily seen that by combining equations (A1) to (A4) that

818 (A6)
$$L^2(\Re^p) = V_j \oplus W_j \oplus W_{j-1} \oplus \cdots$$
$$= \cdots \oplus W_{j+2} \oplus W_{j+1} \oplus W_j \oplus W_{j-1} \oplus W_{j-2} \oplus \cdots$$

819

820 Any square integrable function can be represented by a sum of scaling functions at the
821 largest scale, and a sum of wavelets at all smaller scales. Note that the subspace spanned
822 by the scaling functions at scale *j* contains all subspaces spanned by wavelets at larger
823 scales. This is reflected for the one-dimensional case in equation (8), and is illustrated for
824 a one-dimensional series in Figure A2.

825

826 **Appendix B: Wavelets in Two Dimensions**

827 Following the convention of Mallat (1998), define scaling functions $\Phi^0(x_1,x_2)$ and
828 analyzing wavelets $\Psi^i(x_1,x_2)$ in two-dimensional as

829

830 (B1) $\Psi_{j,k_1,k_2}(x_1,x_2) = 2^{-j}\Psi^i(2^{-j}x_1 - k_1, 2^{-j}x_2 - k_2) \quad j,k_1,k_2 \in \boldsymbol{Z},\ \boldsymbol{i = 1,2,3}$,

831

832 (B2) $\Phi_{j,k_1,k_2}(x_1,x_2) = 2^{-j}\Phi^0(2^{-j}x_1 - k_1, 2^{-j}x_2 - k_2) \quad j,k_1,k_2 \in \boldsymbol{Z}$

833

834 The two dimensional wavelets can be constructed as the tensor product of one-
835 dimensional wavelets and scaling functions at the same scale.

836

837 (B3) $\Psi^1 = \phi(x_1) \cdot \psi(x_2) \equiv \Psi^e(x_1, x_2)$

838

(B4) $\Psi^2 = \psi(x_1) \cdot \phi(x_2) \equiv \Psi^n(x_1, x_2)$

(B5) $\Psi^3 = \psi(x_1) \cdot \psi(x_2) \equiv \Psi^d(x_1, x_2)$

and

(B6) $\Phi^0 = \phi(x_1) \cdot \phi(x_2) \equiv \Phi^s(x_1, x_2)$.

Here $\phi(x_1)$ and $\phi(x_2)$ are the one-dimensional scaling functions in the x_1 and x_2 directions, and $\psi(x_1)$ and $\psi(x_2)$ are the one-dimensional analyzing wavelets in x_1 and x_2. We refer to the functions Ψ^e, Ψ^n, and Ψ^d as the east-west, north-south, and diagonal wavelets. The scaling function in two dimensions $\Phi^0(x_1, x_2)$ is the tensor product of the two one-dimensional scaling functions.

According to Mallat (1998), any square integrable two-dimensional function $g(x_1, x_2)$ can be represented as

(B7)

$$g(x_1,x_2) = \sum_{k_1=-\infty}^{\infty} \sum_{k_2=-\infty}^{\infty} \Phi^s_{j_0,k_1,k_2}(x_1,x_2) c^s_{j_0,k_1,k_2} + \sum_{j=-\infty}^{j_0} \sum_{k_1=-\infty}^{\infty} \sum_{k_2=-\infty}^{\infty} \left[\Psi^e_{j,k_1,k_2}(x_1,x_2) c^e_{j,k_1,k_2} + \Psi^n_{j,k_1,k_2}(x_1,x_2) c^n_{j,k_1,k_2} + \Psi^d_{j,k_1,k_2}(x_1,x_2)\, c^d_{j,k_1,k_2} \right]$$

where j_0 is an arbitrarily scale and $c^s_{j_0,k_1,k_2}, c^e_{j,k_1,k_2}, c^n_{j,k_1,k_2}, c^d_{j,k_1,k_2}$ are coefficients.

Appendix C: A state-space modeling

The data at epoch k, $\underline{d}_k$, are related to the state vector $\underline{x}_k$ through the observation equation which is non-linear because α is included in the state-vector,

(C1) $$\underline{d}_k = \underline{h}_k(\underline{x}_k) + \underline{\varepsilon}_k \qquad \underline{\varepsilon}_k \sim N(0, \underline{\underline{R}}_k).$$

The state vector $\underline{x}_k$ consists of quantities that describe the underlying processes of the system as follows:

(C2) $$x_k = [c_1\ \dot{c}_1 \cdots c_M\ \dot{c}_M, v_1 \cdots v_N, L_1 \cdots L_N, F_1, F_2, \alpha\ ]^T,$$

where M is the number of basis functions and N is the number of stations. $\underline{\varepsilon}_k$ is the measurement errors where $\underline{R}_k = \sigma^2 \underline{\underline{\Sigma}}_{\mathbf{x}}$. The observation equation includes our model for the GPS time series (eq 1). In the NIF, it has sometimes been augmented with additional "pseudo-data" for enforcing positivity or smoothing constraints (*McGuire and Segall, 2003*). However there are no non-linear constraints that need to be enforced in this manner in our current implementation of the NSF.

The state-transition equation propagates the state vector and its covariance matrix forward in time and is a simple linear equation for our chosen stochastic models for L and c.

(C3) $$\begin{aligned} \underline{x}_{k+1|k} &= \underline{\underline{T}}_k \cdot \underline{x}_k + \underline{\delta}_k \qquad \underline{\delta}_k \sim N(0, \underline{\underline{Q}}_k) \\ \Sigma_{k+t|k} &= \underline{\underline{T}}_k \cdot \underline{x}_k \cdot \underline{\underline{T}}_k^T \end{aligned}.$$

Here the matrix $\underline{\underline{T}}_k$ is the state transition matrix that predicts the state of system at epoch k+1 from the previous epoch k, and $\underline{\underline{Q}}_k$ is the covariance matrix of the process noise accounting for statistical variability in the system. These matrices are specified by stochastic process assigned for the various elements of the state vector.

Given the observation equation (C1) and the predicted values of the state vector and its covariance from C3, the extended Kalman filter update equations can be used to encorporate the current data into the estimate of the state vector,

$$\text{(C4)} \quad \underline{x}_{k+1|k+1} = \underline{x}_{k+1|k} + \underline{\underline{K}}_{k+1} \cdot \underline{\nu}_{k+1} \ ,$$

$$\text{(C5)} \quad \underline{\underline{K}}_{k+1} = \underline{\underline{\Sigma}}_{k+1|k} \cdot \underline{\underline{H}}^T_{k+1} \cdot \left(\underline{\underline{R}}_{k+1} + \underline{\underline{H}}_{k+1} \cdot \underline{\underline{\Sigma}}_{k+1|k} \cdot \underline{\underline{H}}^T_{k+1} \right)^{-1}$$

$$\text{(C6)} \quad \underline{\nu}_{k+1} = \underline{d}_k - \underline{h}_{k+1}(\underline{x}_{k+1|k})$$

By iterating the prediction and update steps, one can proceed through the dataset to determine the best estimate of the state vector at each epoch given all of the data up to that point. It is often desireable to determine the best estimate of the state vector at a given epoch given all of the data (from both before and after that epoch). This estimate is determined by effectively running the filter backwards in time using an efficient algorithm known as the Kalman smoother (see *Rauch et al*., 1965; *Segall and Matthews*, 1997). The time series of the transient component deformation shown in figures 8 and 12 are these backsmoothed estimates.

Figure Captions:

Figure 1. One-dimensional Deslauriers-Dubuc interpolation wavelet of degree 3.

905

906 **Figure 2.** An example of the two-dimensional Deslauriers-Dubuc Interpolating wavelet
907 of degree 3 with the scale j = -1. A) East-west analyzing wavelet, Ψ^e ; B) North-south
908 analyzing wavelet, Ψ^n ; and C) Diagonal analyzing wavelet, Ψ^d .

909

910 **Figure 3.** Simulation using the station distribution of the Southern California Integrated
911 GPS Network (SCIGN, black triangles). The black vectors show the distribution of the
912 transient displacement (top) and secular (bottom) at the final epoch at all GPS stations.
913 White arrows give the scale in each plot, note that the magnitude of the secular field is
914 significantly larger than that of the transient field. The two white triangles give the
915 locations of stations BILL and BRAN.

916

917 **Figure 4.** The distribution of wavelet translations used at the different spatial scales used
918 in the SCIGN synthetic test. Small panels show examples of the two-dimensional
919 Deslauriers-Dubuc Interpolating diagonal wavelet functions for the j = 0, -1,-2,-3 scales
920 at a particular translation. The top panel shows the positions of various translations that
921 were selected for the inclusion in the state vector based on the selection criteria for being
922 well observed. The different color circles indicate different scales, j (red = 0, magenta = -
923 1, green = -2, cyan = -3). Black triangles indicate the location of the GPS stations. Note
924 that there are fewer wavelets where the station density is sparse. Each horizontal axis is
925 regularized to a dyadic scale.

926

927 **Figure 5.** The model norm of the transient strain field at the final epoch for the synthetic

928 dataset as estimated by the filter for different values of the spatial smoothing parameter λ^2.

929

930 **Figure 6.** Estimated values of α determined by the forward run of the filter on the
931 synthetic dataset as a function of epoch for various values of λ^2. When the spatial
932 damping is too small (e.g., λ^2=0.001) the filter immediately increases the value of α to
933 allow the secular field to be mapped into the transient term. For more appropriate values
934 of λ^2 the estimate of α decreases (as the filter accumulates evidence of the lack of a
935 transient) until the transient displacement rate reaches its peak (between epochs ~75-100)
936 when the estimate of α is forced to increase abruptly by the data.

937

938 **Figure 7**. The estimated transient displacement field at the final epoch for a value of
939 λ^2=0.05 (top left panel) just below the inflection point in Figure 5, and for a value at the
940 inflection point (λ^2=0.1, top right panel). In the left panel, the transient signal is highly
941 contaminated by the (much larger real amplitude) secular field, whereas for the
942 appropriate choice of λ^2 the estimated transient agrees well with the input transient
943 (compare to Figure 3). The lower panels show the estimated secular field for each value
944 of λ^2.

945

946 **Figure 8.** Synthetic GPS time series for the stations BILL and BRAN shown in Figure 3.
947 The filtered estimate of the secular velocity has been subtracted from the synthetic data
948 (blue asterisks). The black curve denotes the back-smoothed estimate of the transient
949 displacement, and the green curve denotes the estimated benchmark term for each
950 component. The red curve is the sum of the black and green curves and shows the overall

fit to the data.

Figure 9. The 1996 Boso Peninsula transient event. Map showing the transient displacement field estimated by differencing the mean station positions from one month of data before and after the event (red arrows) and the transient displacement field estimated by the filter at the final epoch (black arrows). Stations CHIO, CHOE, OOAM, and TOMI are shown as a square, triangle, circle, and diamond respectively.

Figure 10. The model norm of the transient strain field at the final epoch for the Boso dataset as estimated by the filter for different values of the spatial smoothing parameter λ^2.

Figure 11. The estimate of α determined by the forward run of the filter on the Boso dataset as a function of epoch for various values of λ^2.

Figure 12. Time series of displacement at four GEONET stations (CHIO, CHOE, OOAM, TOMI) in east (up) and north (bottom) for raw data (blue dots) and transient signal (black line), benchmark motion (green line) as in Figure 8. See Figure 9 for the location of the stations. The red line is the sum of the black and green curves and shows the fit to the data.

Figure A-1. Schematic relation of subspaces between scaling functions and analyzing wavelets. Note that the subspace spanned by the scaling functions at scale j - 1, V_{j-1} is equivalent to that spanned by the scaling functions V_j and analyzing wavelets W_j at scale j.

974

975 **Figure A-2.** An example of the relationship between scaling functions and analyzing
976 wavelets. The original signal consisting of 2^8 data points is decomposed into subspaces
977 spanned by a scaling function V_{-7} and analyzing wavelet W_{-7} at scale j = –7. The
978 subspace V_{-7} can be further decomposed into larger spatial scale components. For
979 example, the signal can be represented by a scaling function V_{-6}, and analyzing wavelet
980 components W_{-6} and W_{-7}. The scaling function V_{-6} can be further subdivided such that
981 the signal is represented by a scaling function V_{-5}, and analyzing wavelet components
982 W_{-5}, W_{-6}, and W_{-7}.

983

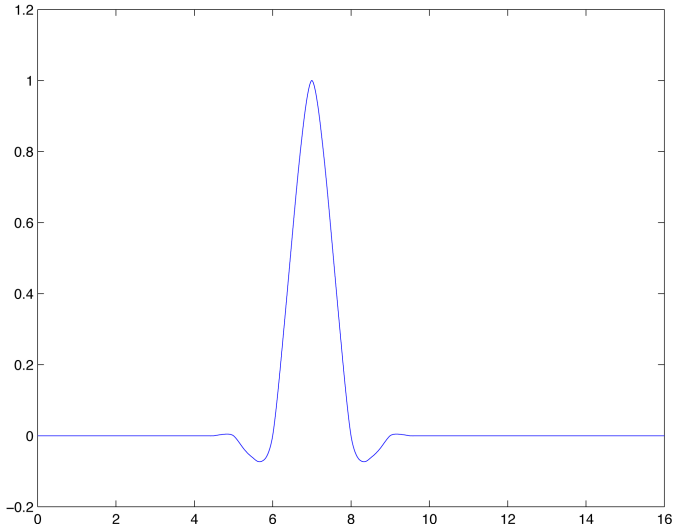

Figure 1.

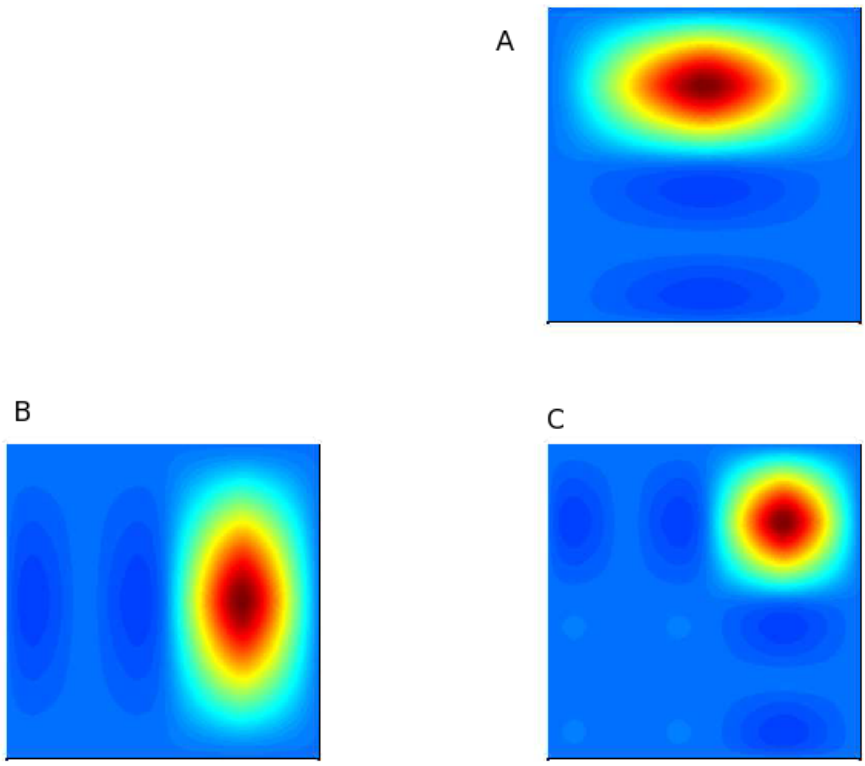

989

990 Figure 2.

991

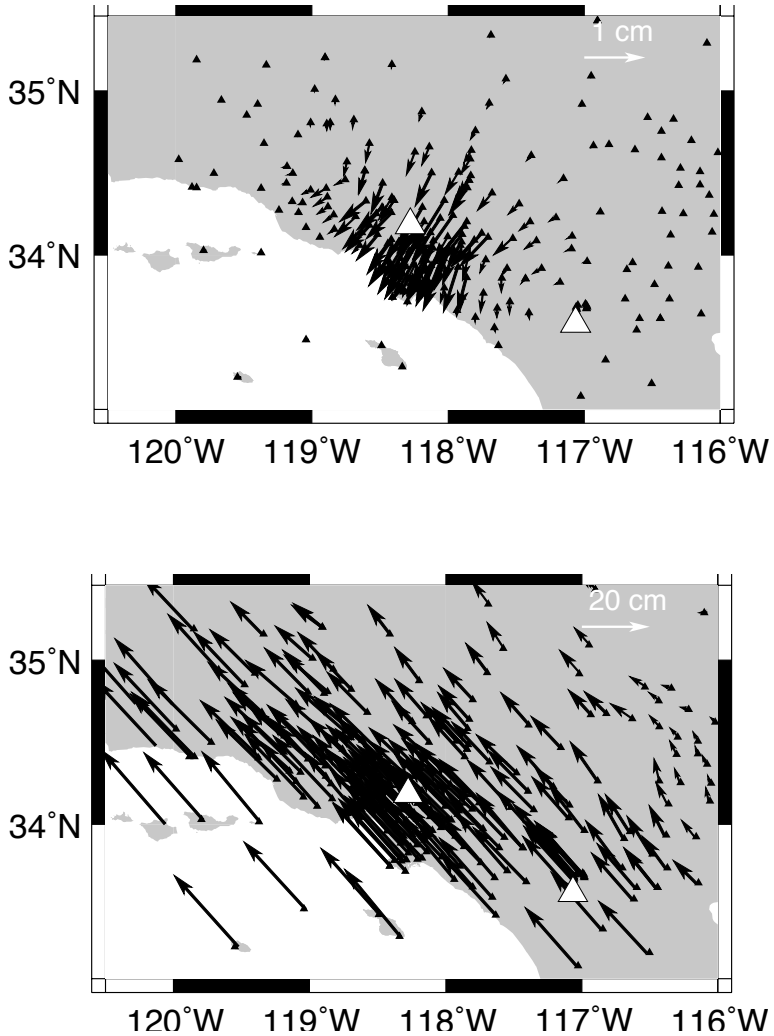
1 cm
35˚N
34˚N
120˚W
119˚W
118˚W
117˚W
116˚W
20 cm
35˚N
34˚N
120˚W
119˚W
118˚W
117˚W
116˚W

Figure 3.

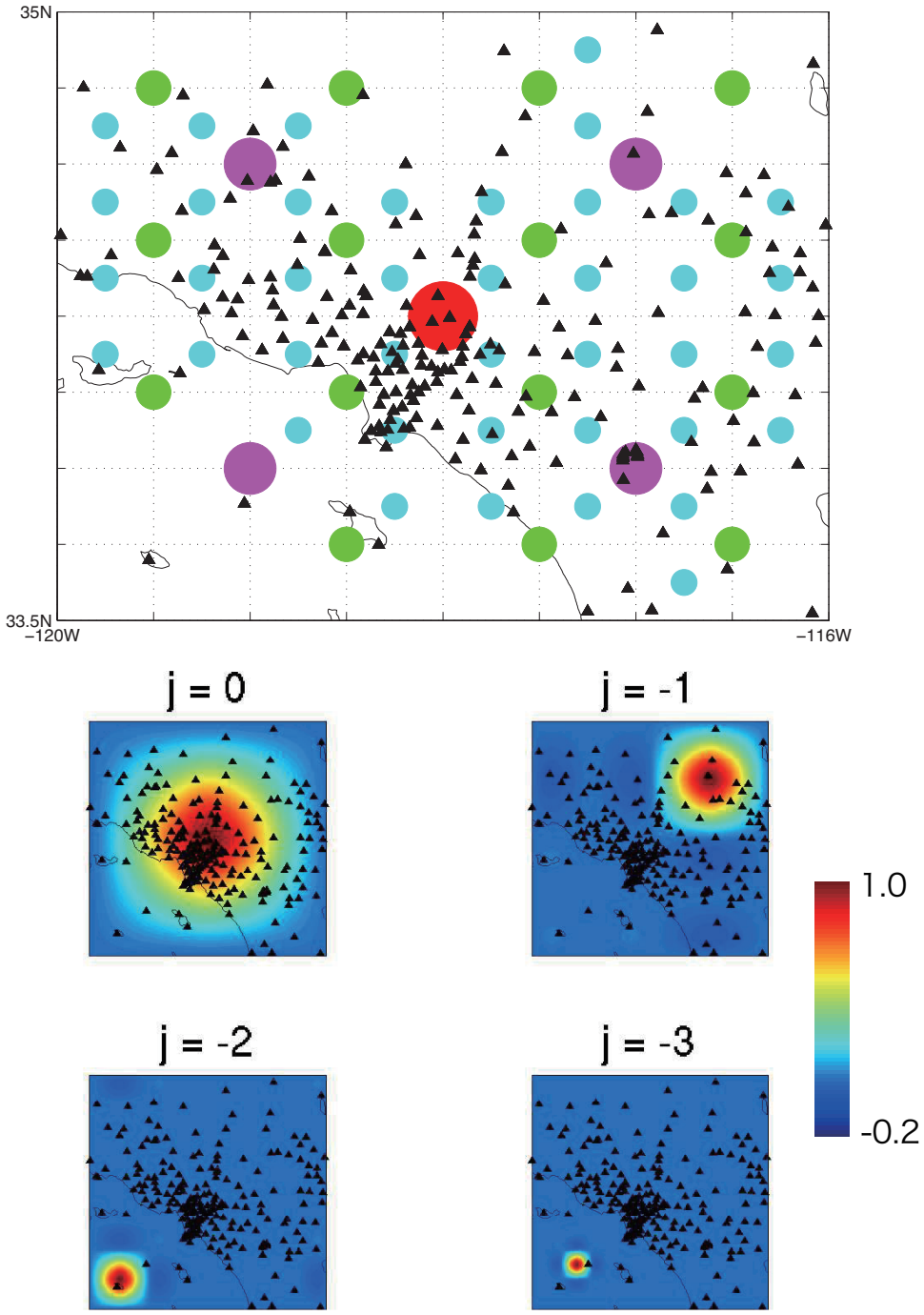

Figure 4.

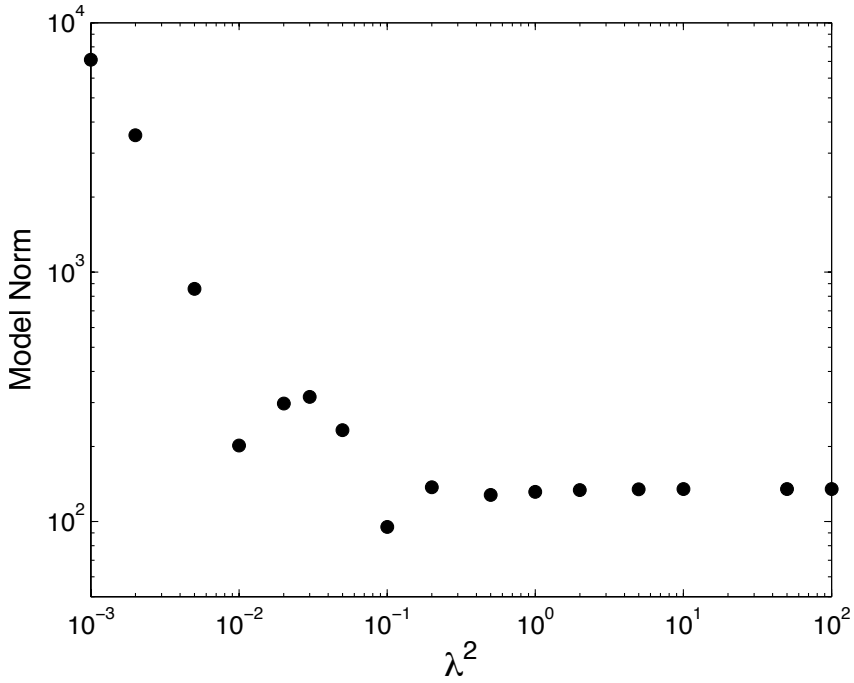
Model Norm
10^4
10^3
10^2
10^{-3}
10^{-2}
10^{-1}
10^0
10^1
10^2
λ^2

Figure 5

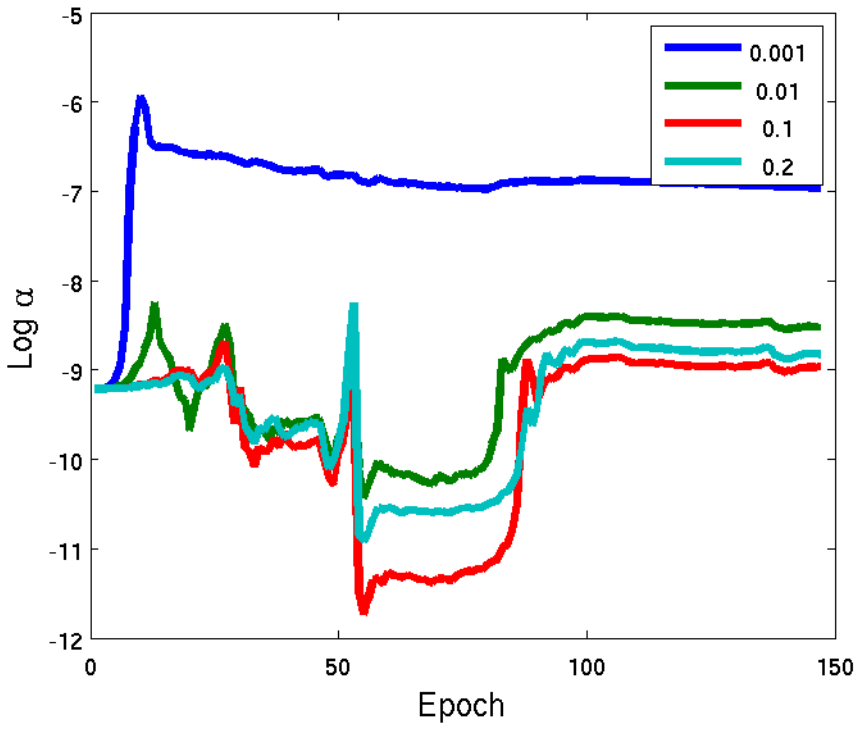
Log α
Epoch
0.001
0.01
0.1
0.2
-5
-6
-7
-8
-9
-10
-11
-12
0
50
100
150

1007 Figure 6.

1008

1009

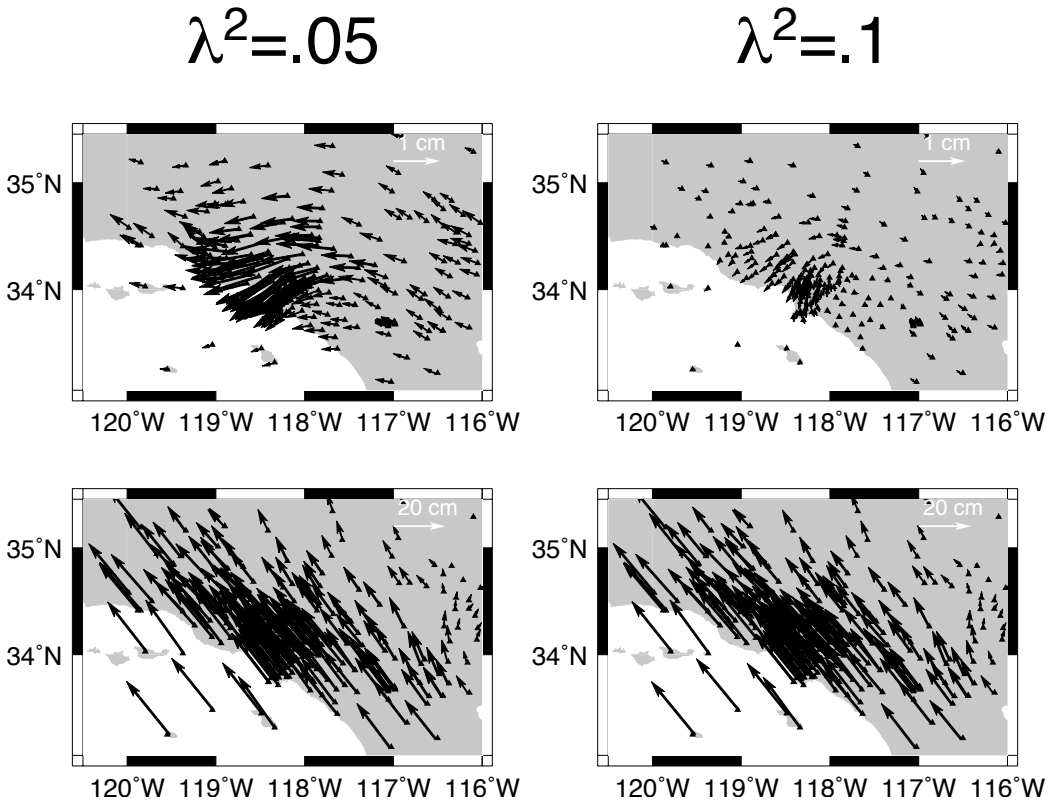

1009

1010

1011 Figure 7.

1012

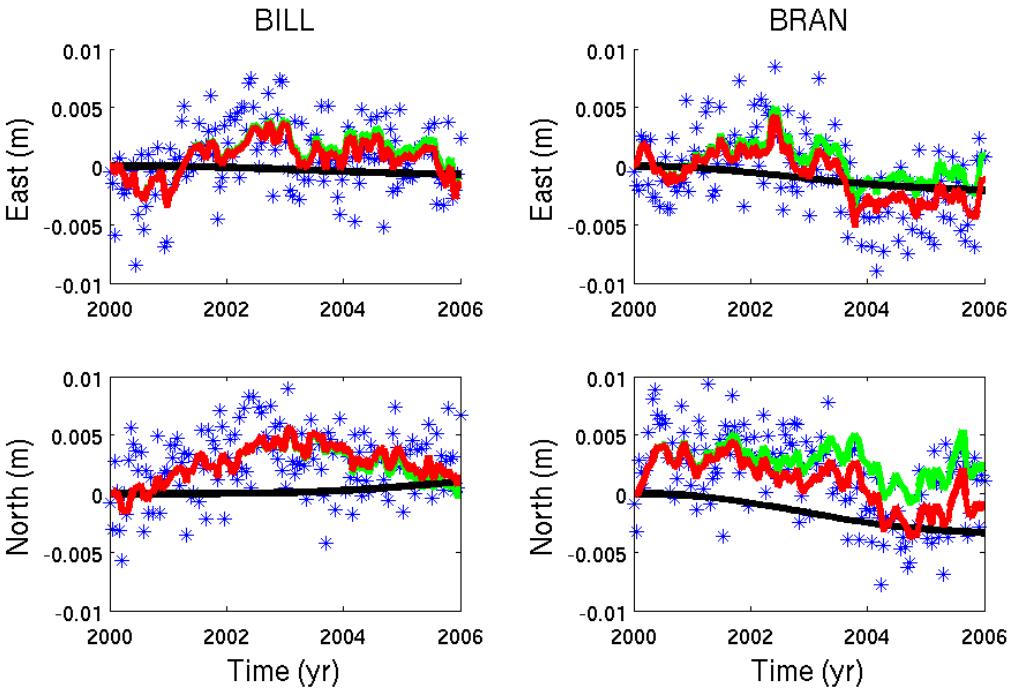

1013

1014

1015 Figure 8.

1016

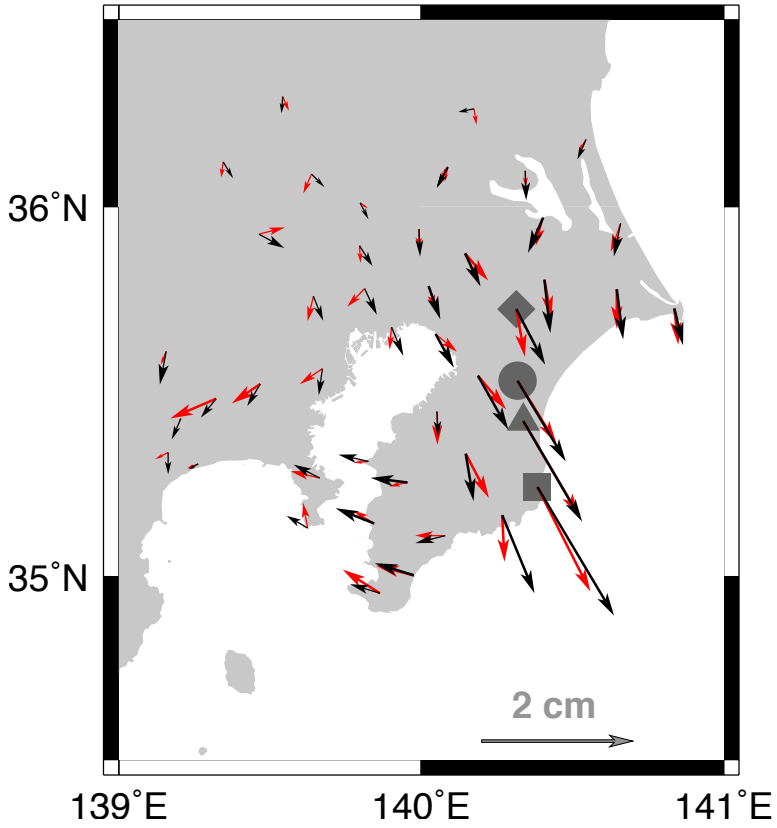

1017

1018

1019 Figure 9

1020

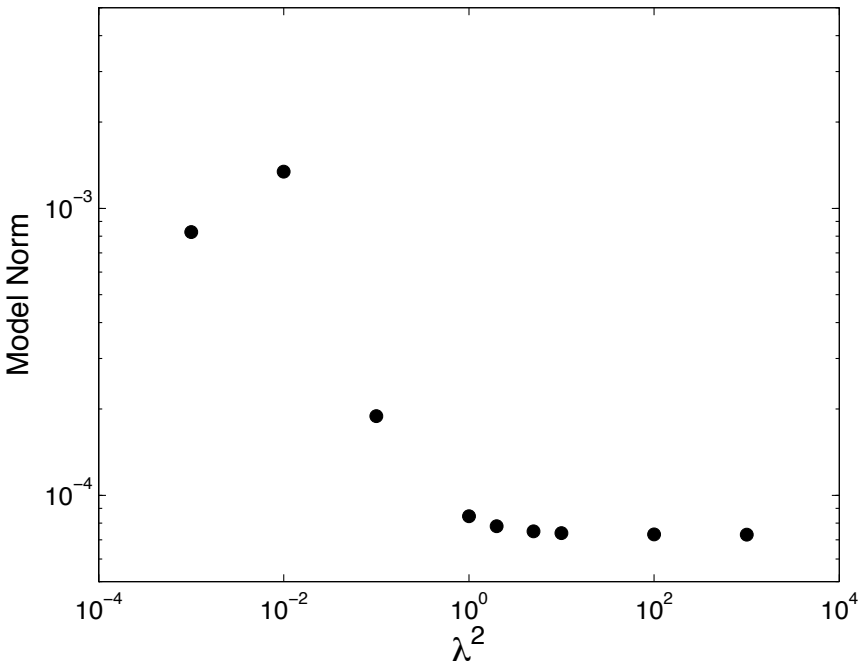

Figure 10.

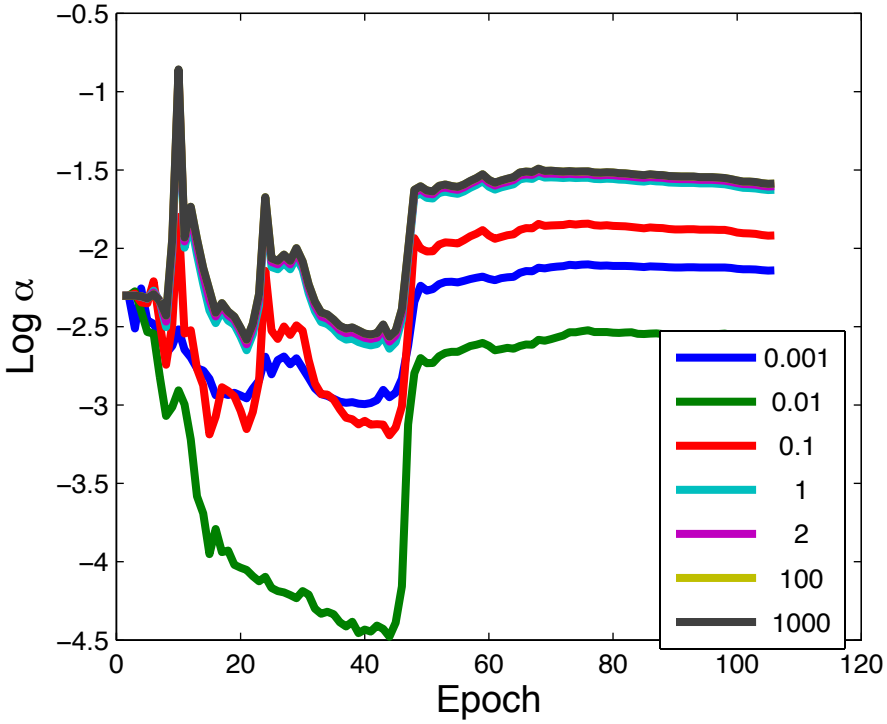
−0.5
−1
−1.5
−2
−2.5
−3
−3.5
−4
−4.5
Log α
0
20
40
60
80
100
120
Epoch
0.001
0.01
0.1
1
2
100
1000

Figure 11.

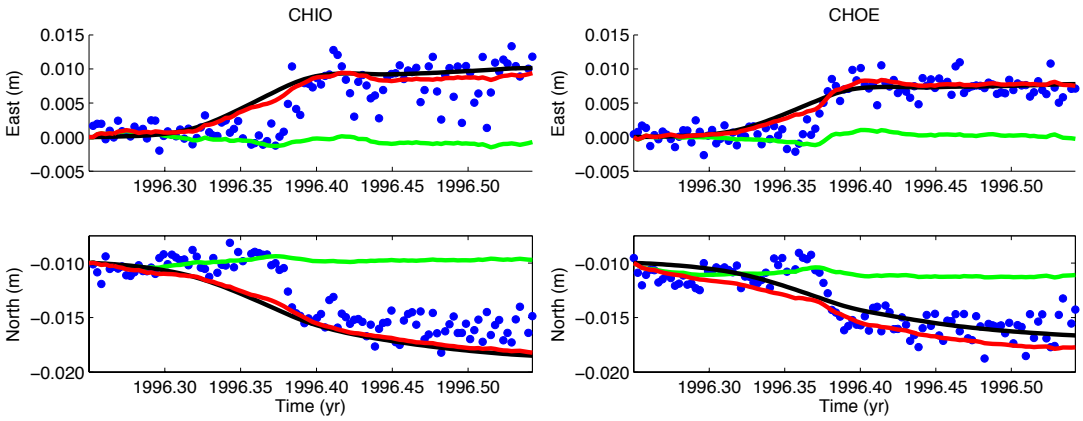
CHIO
CHOE
East (m)
North (m)
0.015
0.010
0.005
0.000
−0.005
−0.010
−0.015
−0.020
1996.30
1996.35
1996.40
1996.45
1996.50
Time (yr)

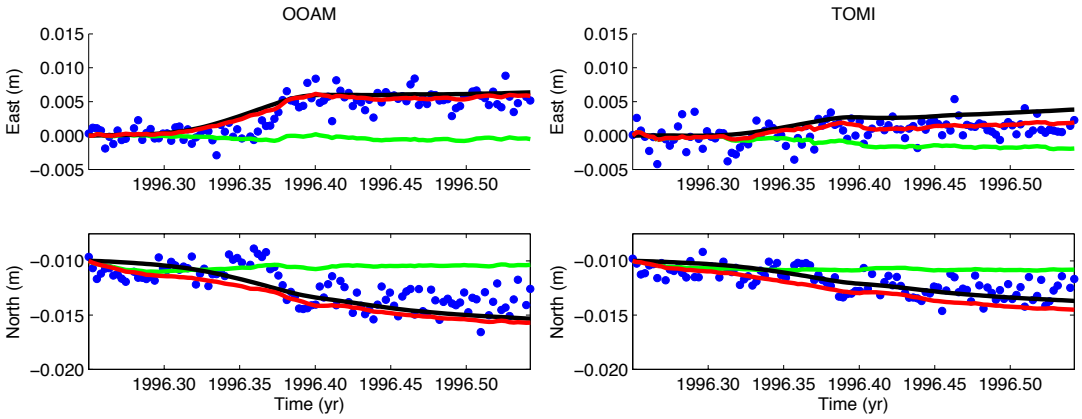
OOAM
TOMI
East (m)
North (m)
0.015
0.010
0.005
0.000
−0.005
−0.010
−0.015
−0.020
1996.30
1996.35
1996.40
1996.45
1996.50
Time (yr)

Figure 12.

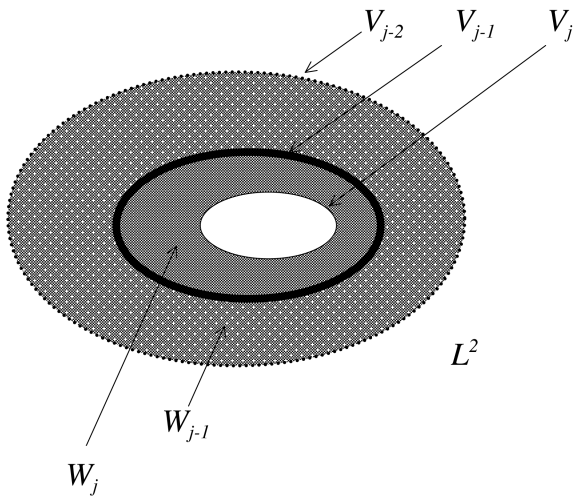

1035

1036 Figure A1.

1037

1038

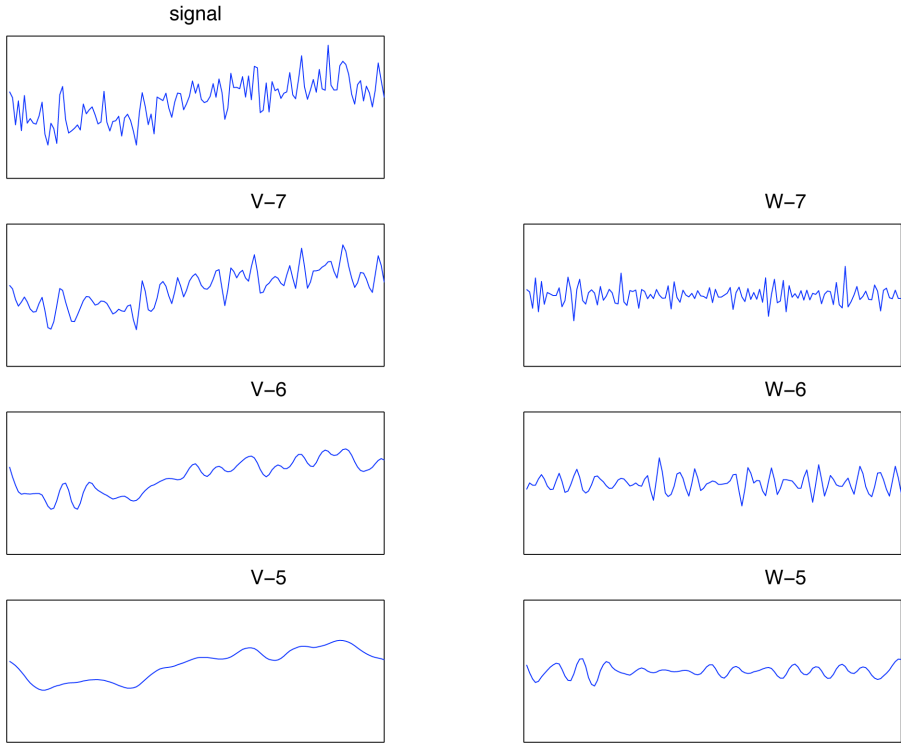

1039

1040 Figure A2.

1041